Activating inert non-defect sites in Bi catalysts using tensile strain engineering for highly active CO_2 electroreduction

Xingbao Chen[1,2,7], Ruihu Lu[2,7], Chengbo Li[3,7], Wen Luo[1,*], Ruohan Yu[1], Jiexin Zhu[1,2,*], Lei Lv[1], Yuhang Dai[1], Shanhe Gong[4], Yazhou Zhou[5], Weiwei Xiong[1], Jiahao Wu[1], Hongwei Cai[1], Xinfei Wu[1], Zhaohui Deng[1], Boyu Xing[1], Lin Su[6], Feiyue Wang[1], Feiyang Chao[1], Wei Chen[1], Chuan Xia[3], Ziyun Wang[2,*], Liqiang Mai[1,*]

[1]State Key Laboratory of Advanced Technology for Materials Synthesis and Processing, Wuhan University of Technology, Wuhan 430070, Hubei, P. R. China.

[2]School of Chemical Sciences, University of Auckland, Auckland, 1010, New Zealand.

[3]School of Materials and Energy, University of Electronic Science and Technology of China, Chengdu 611731, P. R. China.

[4]School of the Environment and Safety Engineering, Jiangsu University, Zhenjiang 212013, P. R. China.

[5]Nanotechnology Centre, Centre for Energy and Environmental Technologies (CEET), VŠB─Technical University of Ostrava, 17. listopadu 2172/15, Ostrava-Poruba 708 00, Czech Republic.

[6]The Southeast University, Nanjing 210000, Jiangsu, P. R. China

[7]These authors contributed equally to this work.

*Email: luowen_1991@whut.edu.cn; jxzhu@whut.edu.cn; ziyun.wang@auckland.ac.nz; mlq518@whut.edu.cn

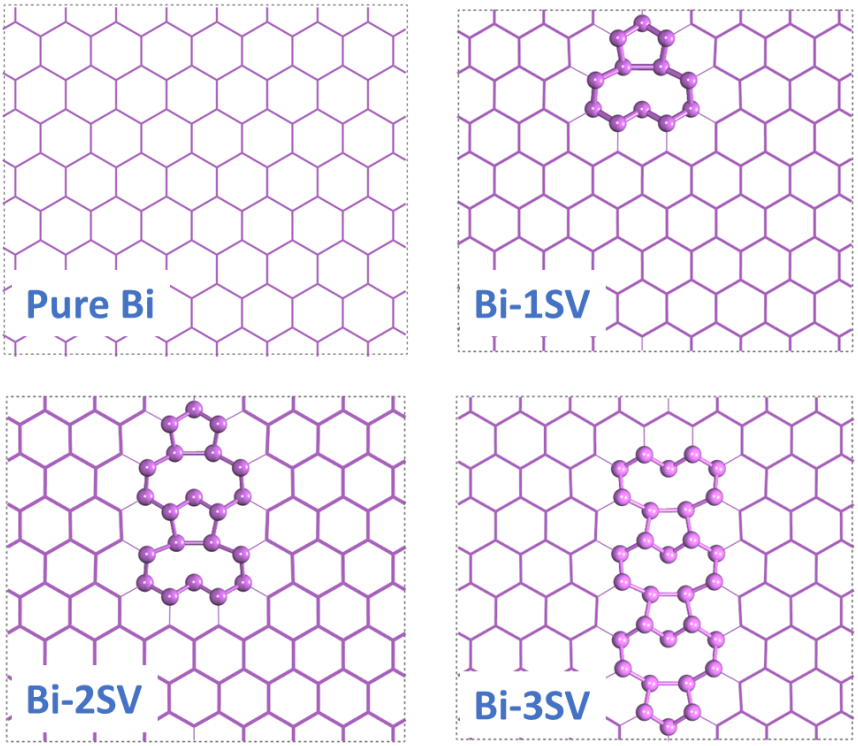

Supplementary Fig. 1| Models of Pure Bi, Bi-1SV, Bi-2SV, and Bi-3SV. The purple lines represent Bi-Bi bonds. The purple spheres highlight SV sites.

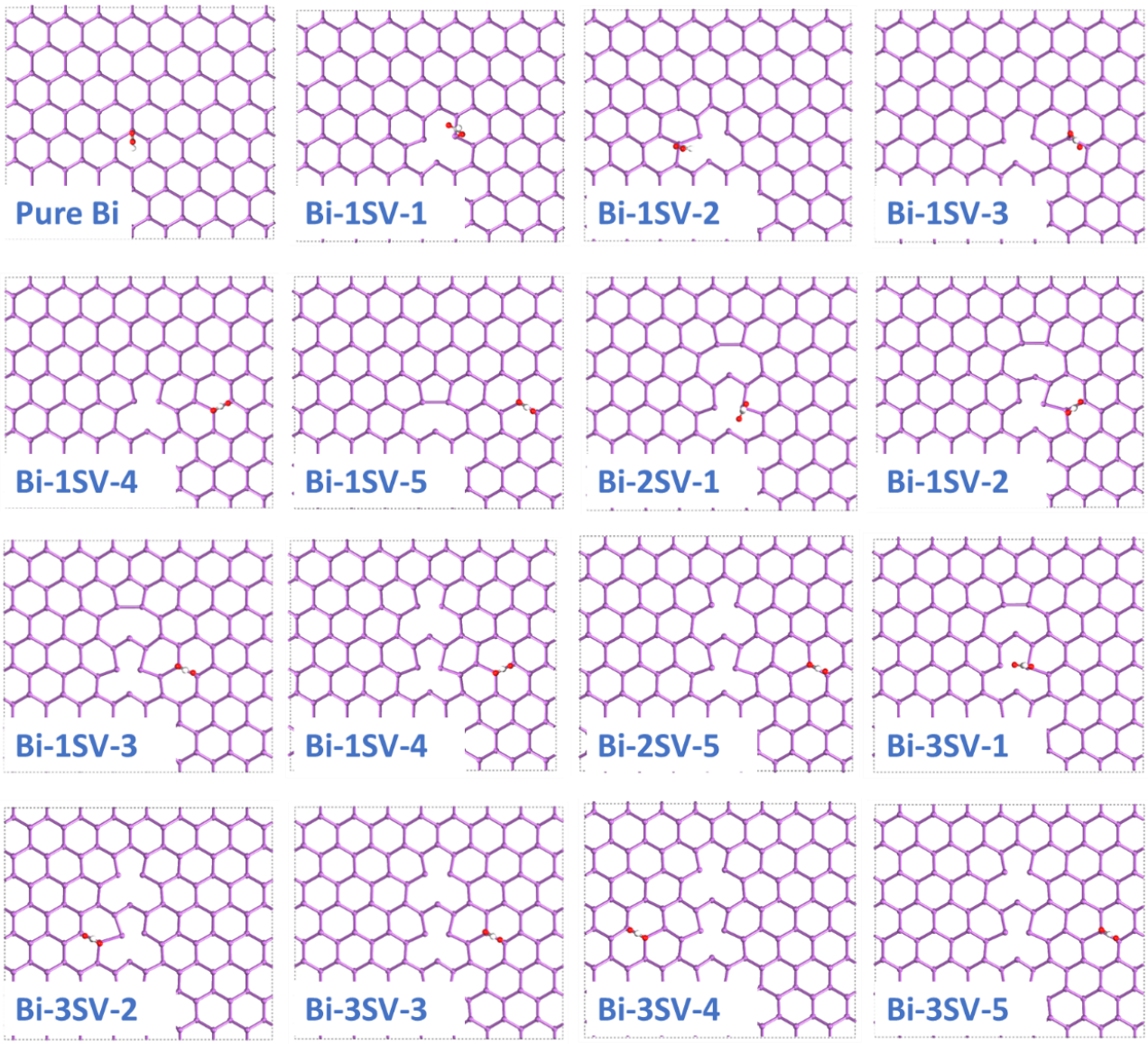

Supplementary Fig. 2| Models of *OCHO adsorption on Bi sites of various Bi catalysts. The white, grey, red, and purple spheres represent H, C, O, and Bi atoms. Respectively.

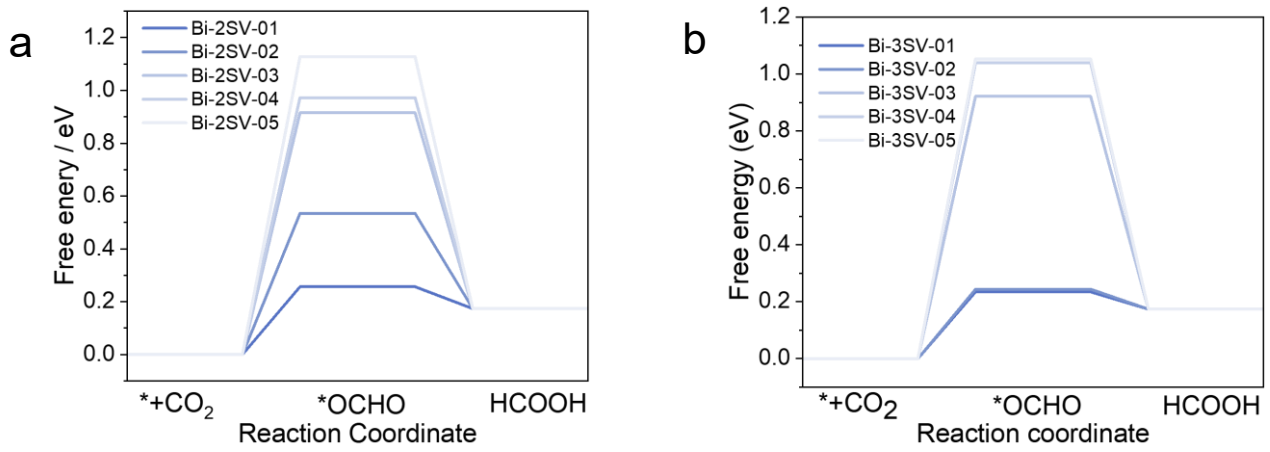

Supplementary Fig. 3| Free energy profile of CO_2RR towards HCOOH on various Bi sites. (a) Bi-2SV sites, (b) Bi-3SV sites. Source data are provided as a Source Data file.

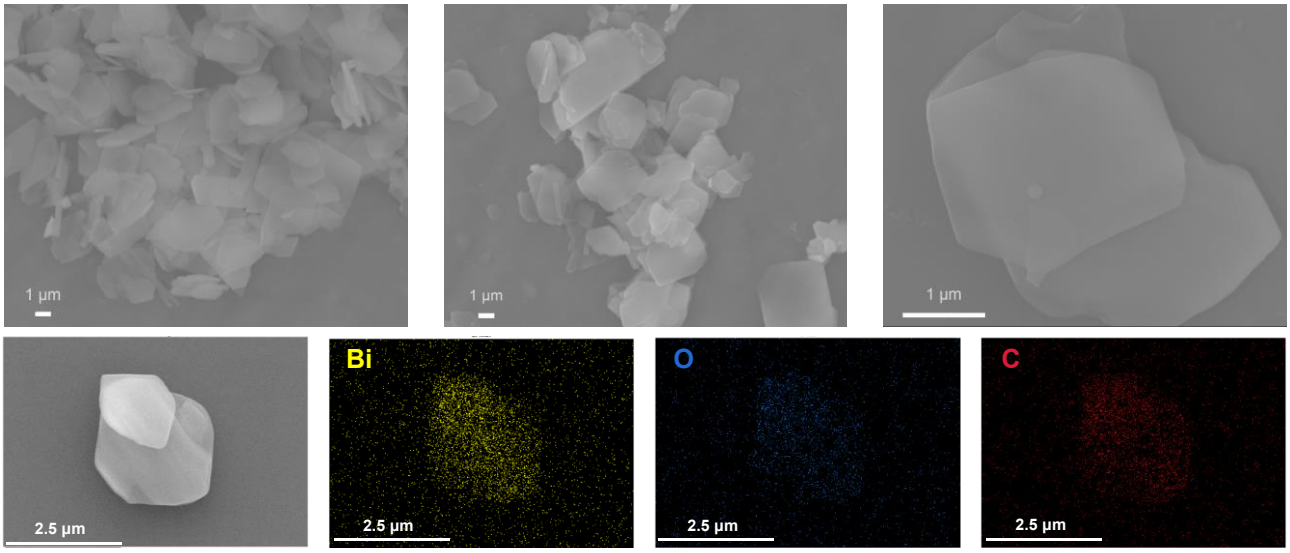

Supplementary Fig. 4| SEM images and EDS mappings of Bi-MOF.

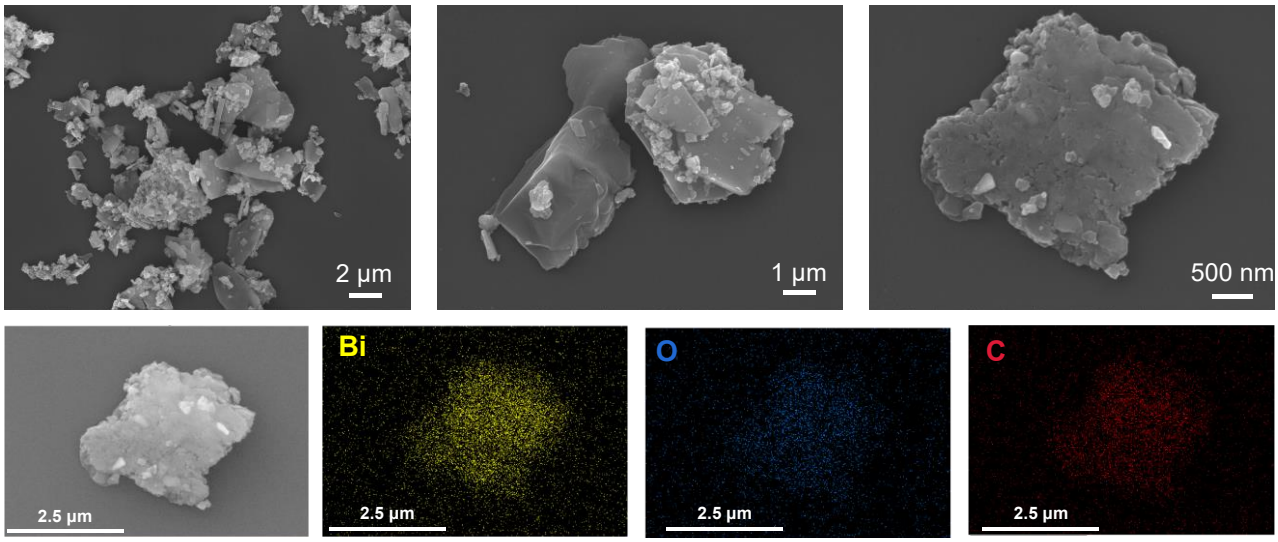

Supplementary Fig. 5| SEM images and EDS mappings of Bi-MOF-MF.

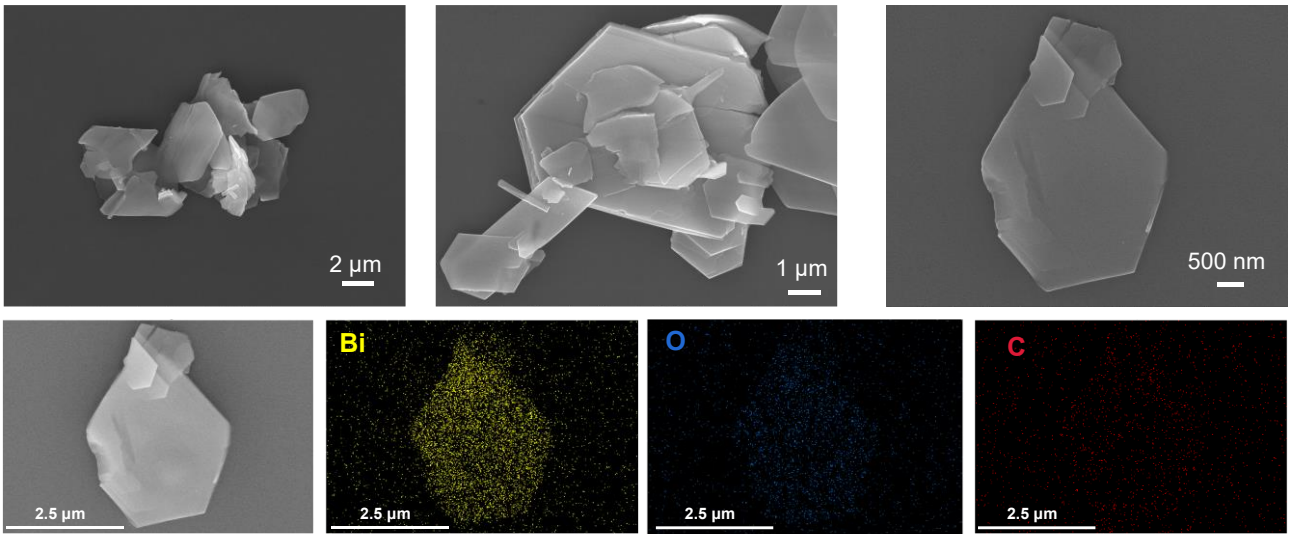

Supplementary Fig. 6| SEM images and EDS mappings of Bi-MOF-TS.

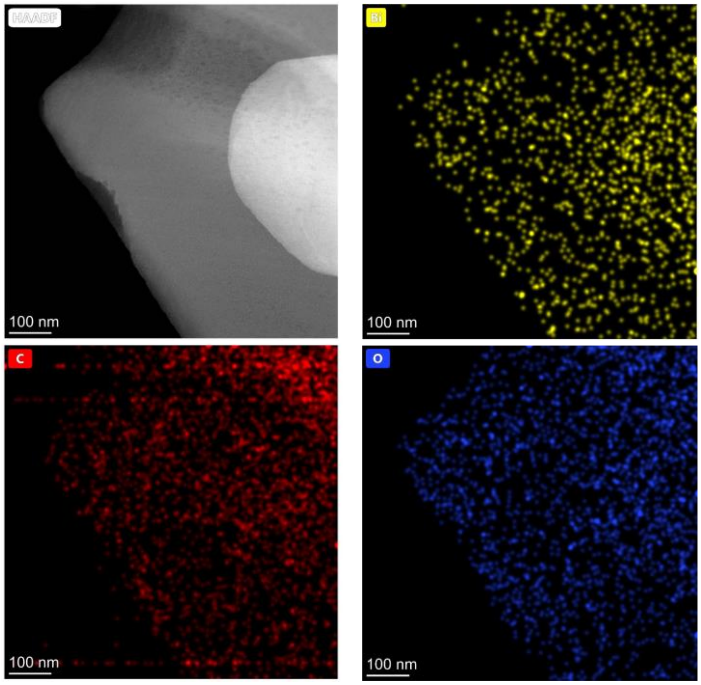

Supplementary Fig. 7| High-angle annular dark-field scanning transmission electron microscopy (HAADF-STEM) image and Energy Dispersive X-ray spectroscopy (EDX) mapping of the Bi-MOF.

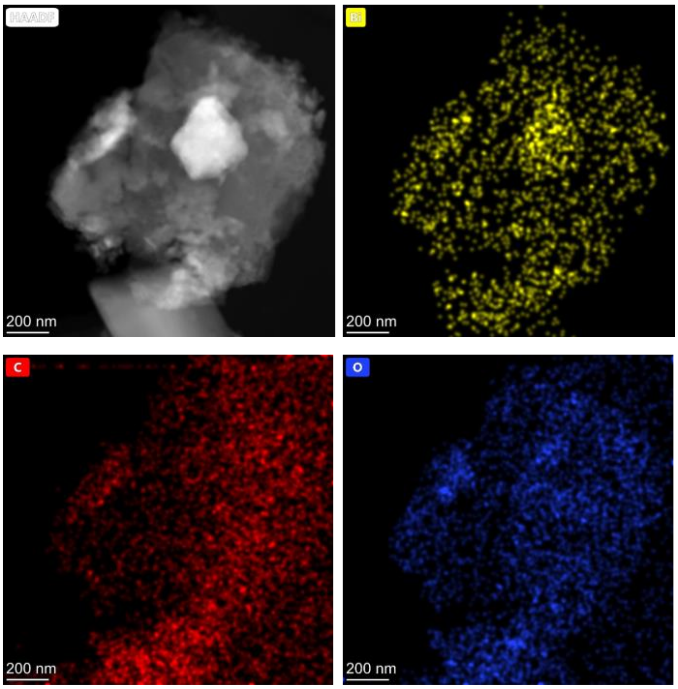

Supplementary Fig. 8| High-angle annular dark-field scanning transmission electron microscopy (HAADF-STEM) image and Energy Dispersive X-ray spectroscopy (EDX) mapping of the Bi-MOF-MF.

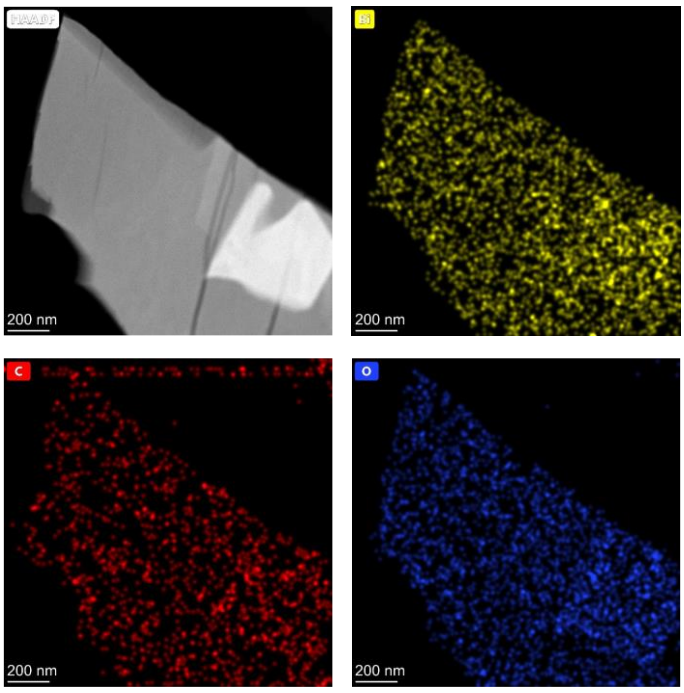

Supplementary Fig. 9| High-angle annular dark-field scanning transmission electron microscopy (HAADF-STEM) image and Energy Dispersive X-ray spectroscopy (EDX) mapping of the Bi-MOF-TS.

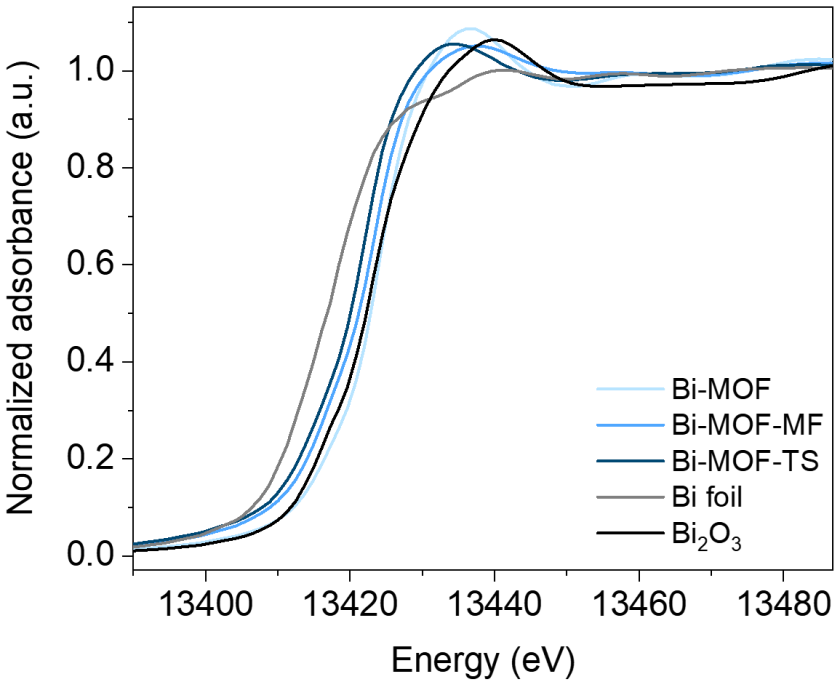

Supplementary Fig. 10| Bi L_3-edge XANES spectra of Bi-MOF, Bi-MOF-MF and Bi-MOF-TS. Source data are provided as a Source Data file.

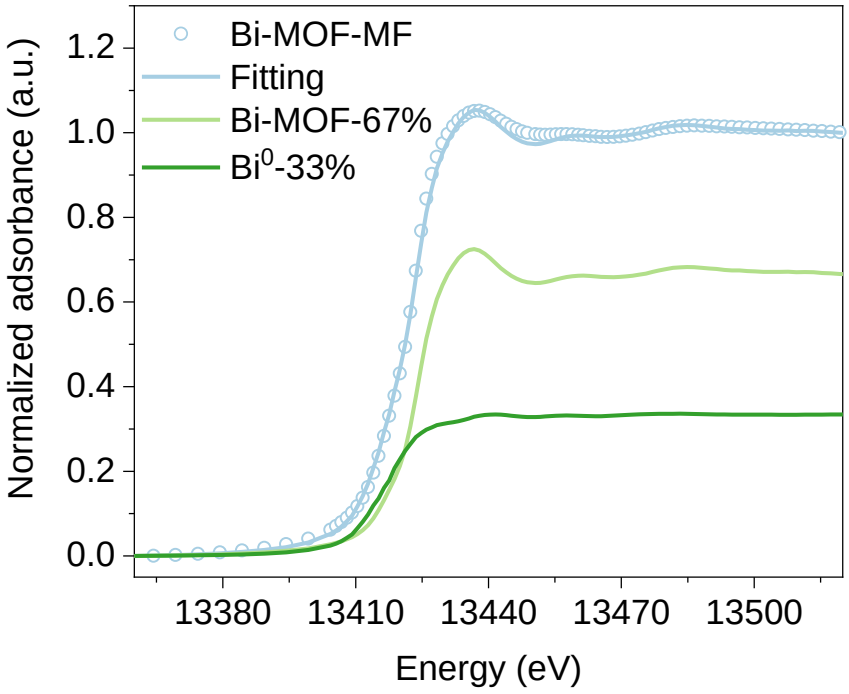

Supplementary Fig. 11| Linear combination analysis of Bi-MOF-MF. Source data are provided as a Source Data file.

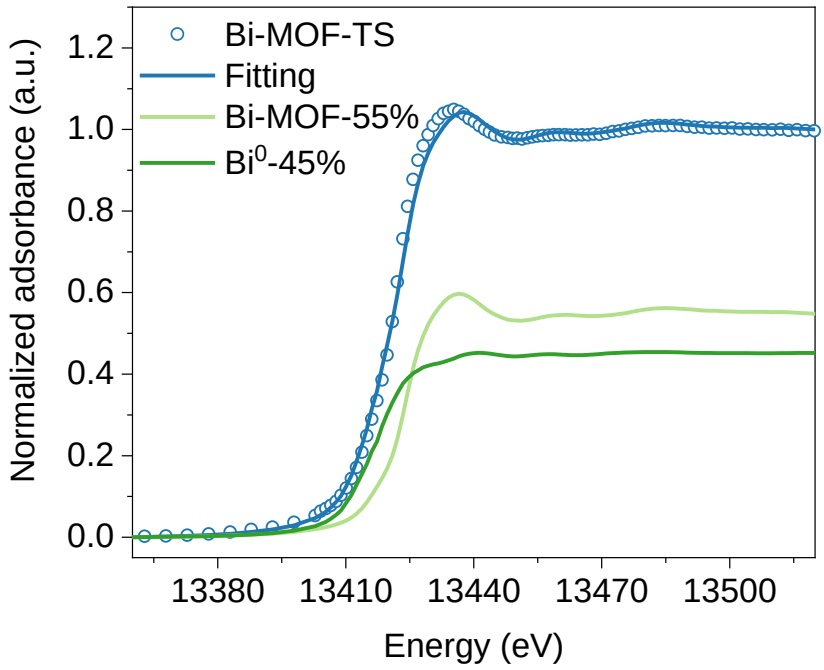

Supplementary Fig. 12| Linear combination analysis of Bi-MOF-TS. Source data are provided as a Source Data file.

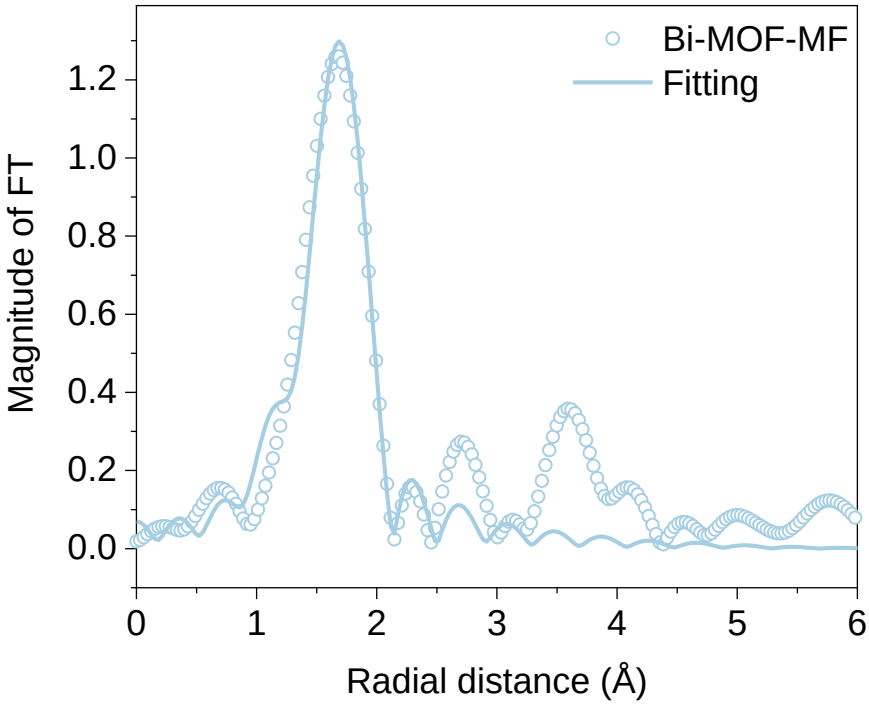

Supplementary Fig. 13| EXAFS fitting of Bi-MOF-MF. Source data are provided as a Source Data file.

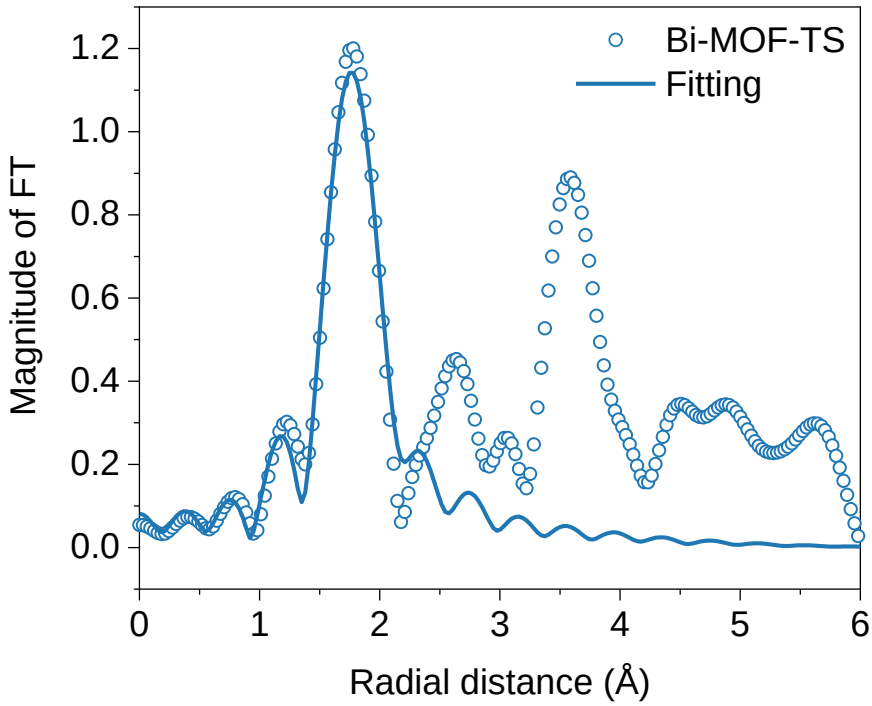

Supplementary Fig. 14| EXAFS fitting of Bi-MOF-TS. Source data are provided as a Source Data file.

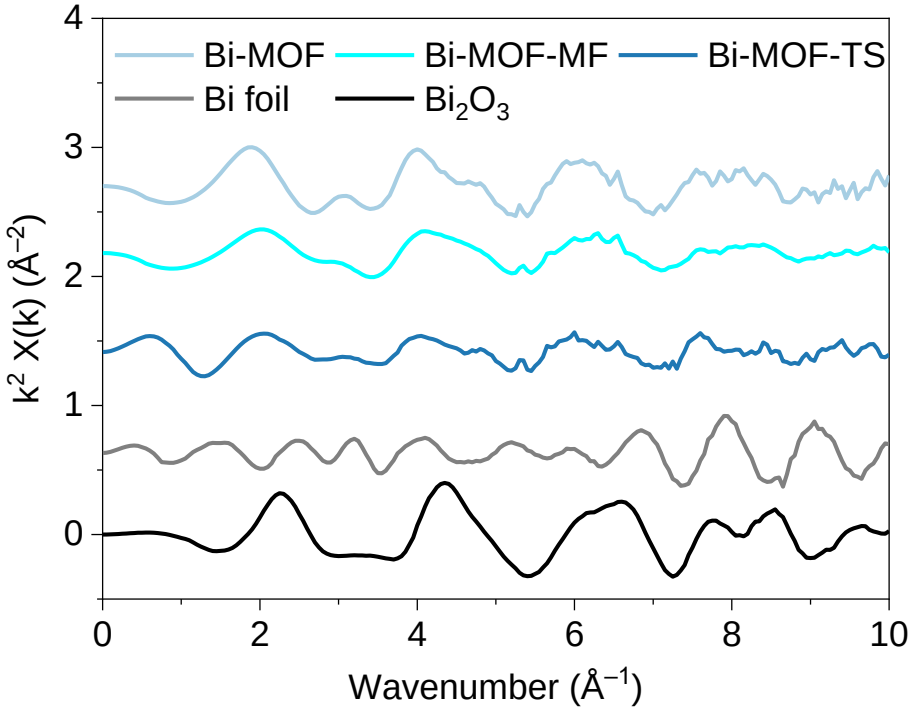

Supplementary Fig. 15| K-space of Bi-MOF, Bi-MOF-MF, Bi-MOF-TS, referenced Bi foil and Bi_2O_3. Source data are provided as a Source Data file.

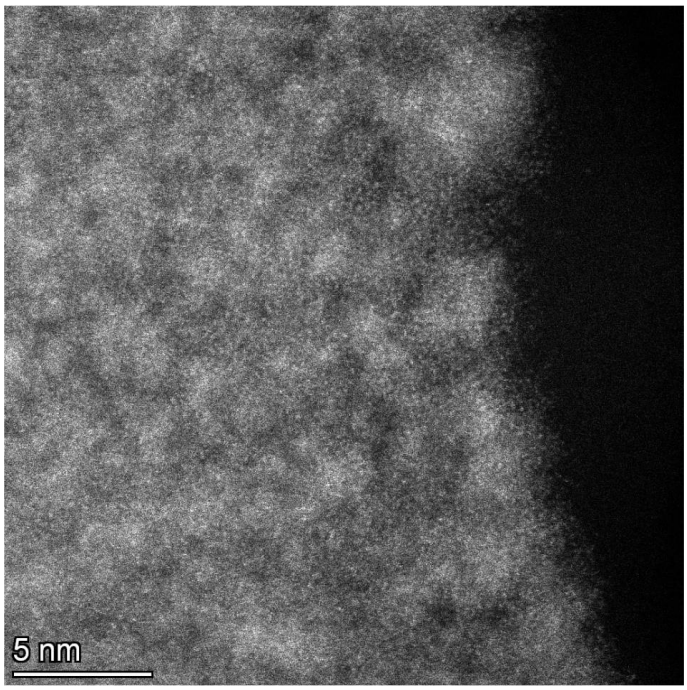

Supplementary Fig. 16| HAADF-STEM image of Bi-MOF.

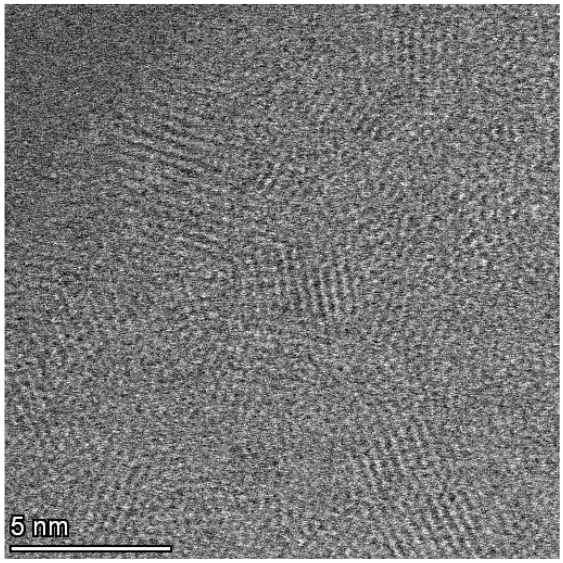

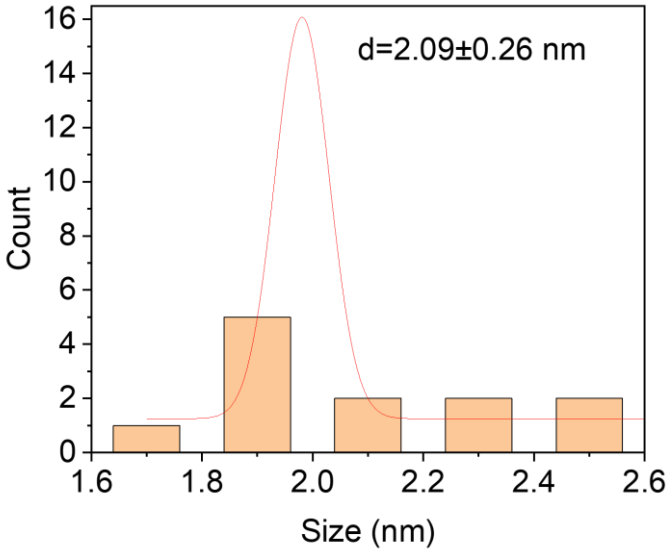

Supplementary Fig. 17| HAADF-STEM image of Bi-MOF-TS and the size distribution for Bi_2O_3 clusters in it.

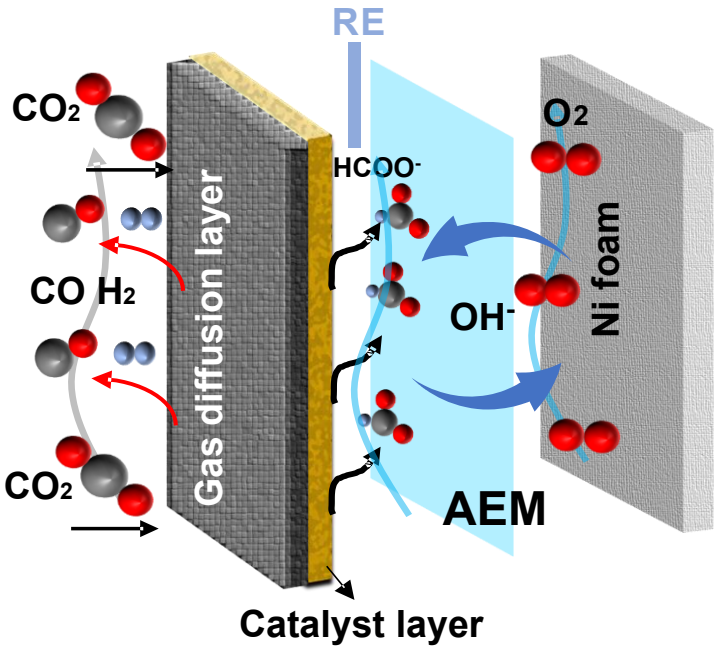

Supplementary Fig. 18| Schematic representation of alkaline gas diffusion electrode system.

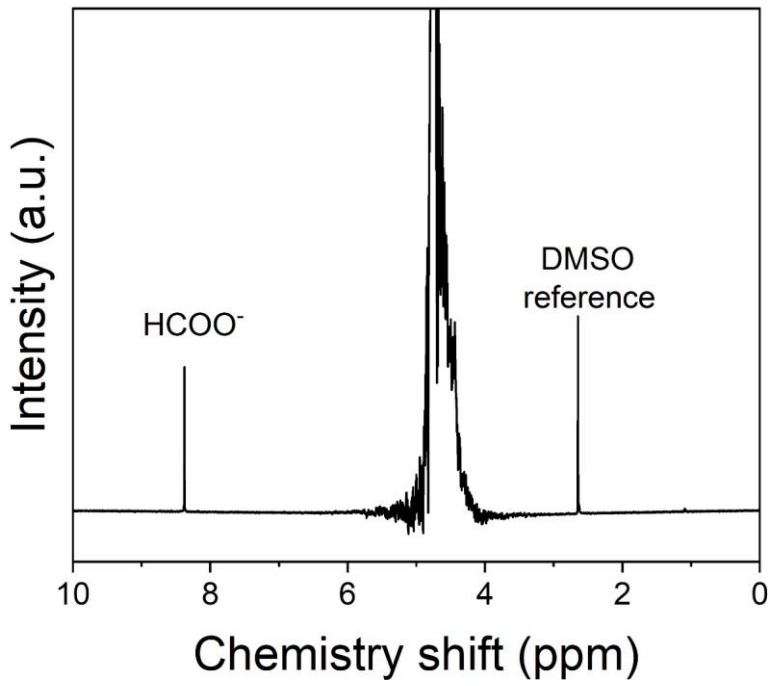

Supplementary Fig. 19| NMR spectrum of the liquid product in flow-cell test. Source data are provided as a Source Data file.

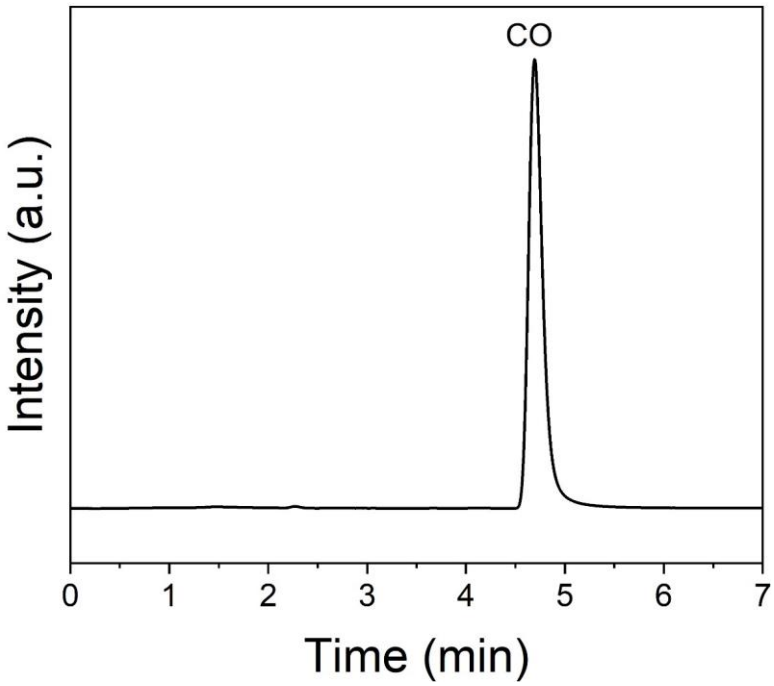

Supplementary Fig. 20| GC FID1 spectrum of the gas product in flow-cell test. Source data are provided as a Source Data file.

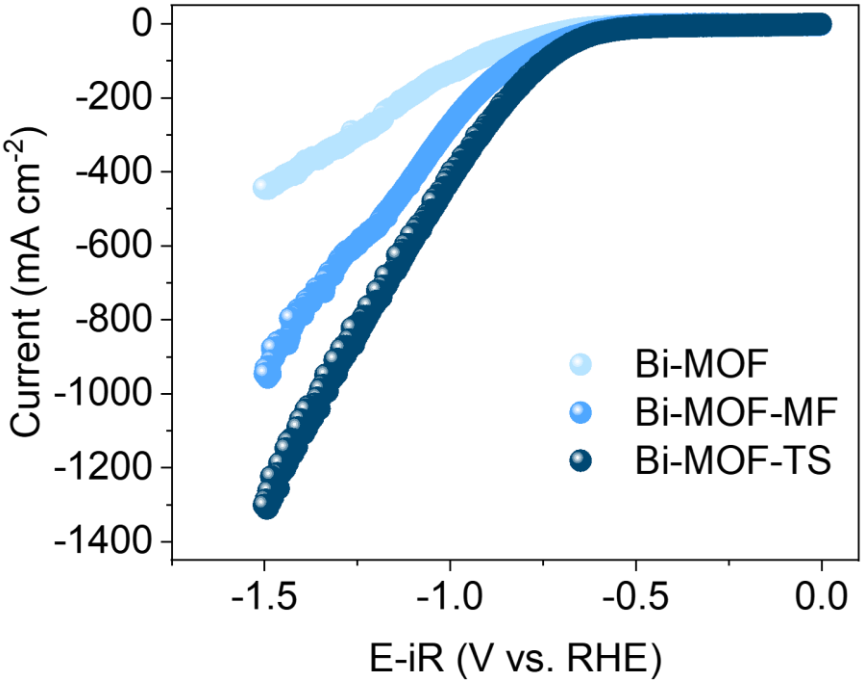

Supplementary Fig. 21| LSV curves of Bi-MOF, Bi-MOF-MF and Bi-MOF-TS in 1 M KOH electrolyte at the rate of 10 mV cm^{-1}. 3 Ω iR correction was applied. Source data are provided as a Source Data file.

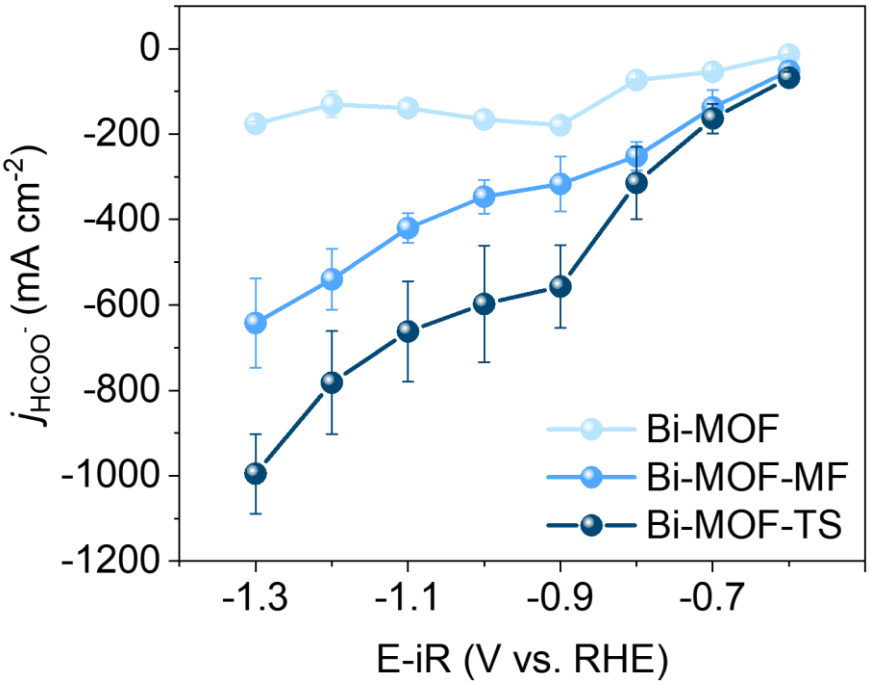

Supplementary Fig. 22| Partial current density of $HCOO^-$ under different applied currents for Bi-MOF, Bi-MOF-MF and Bi-MOF-TS in alkaline electrolyte. 3 Ω iR correction was applied. Source data are provided as a Source Data file.

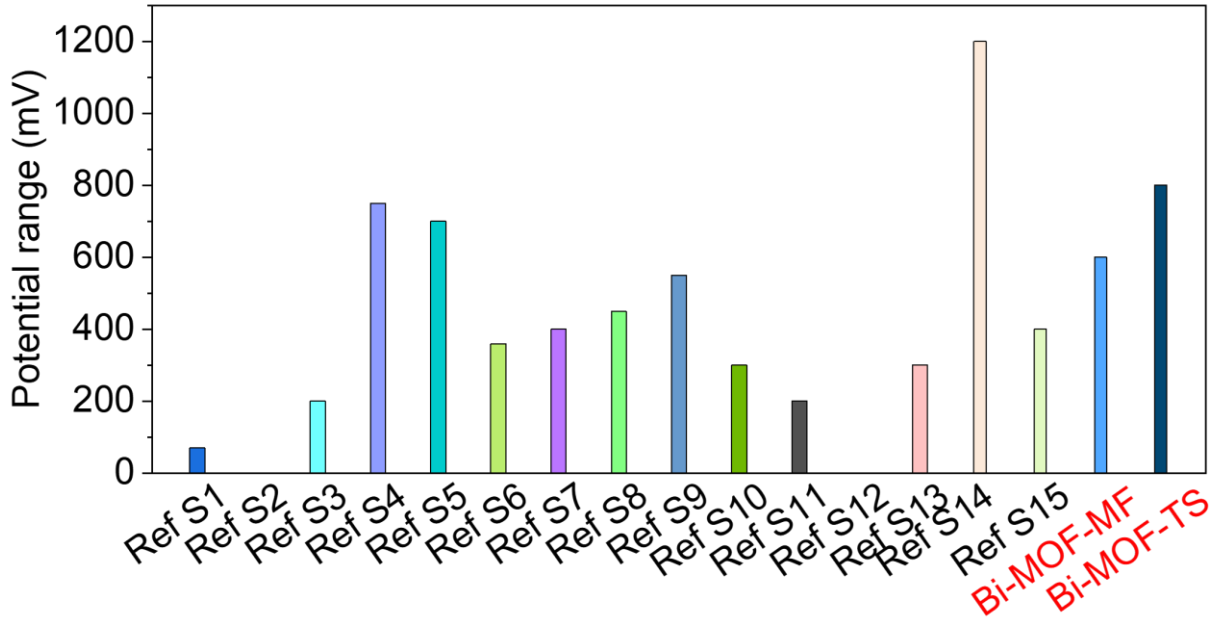

Supplementary Fig. 23| Comparison of the potential range with formate selectivity over 90% for Bi-MOF-MF, Bi-MOF-TS and recently reported Bi-based catalysts. Source data are provided as a Source Data file.

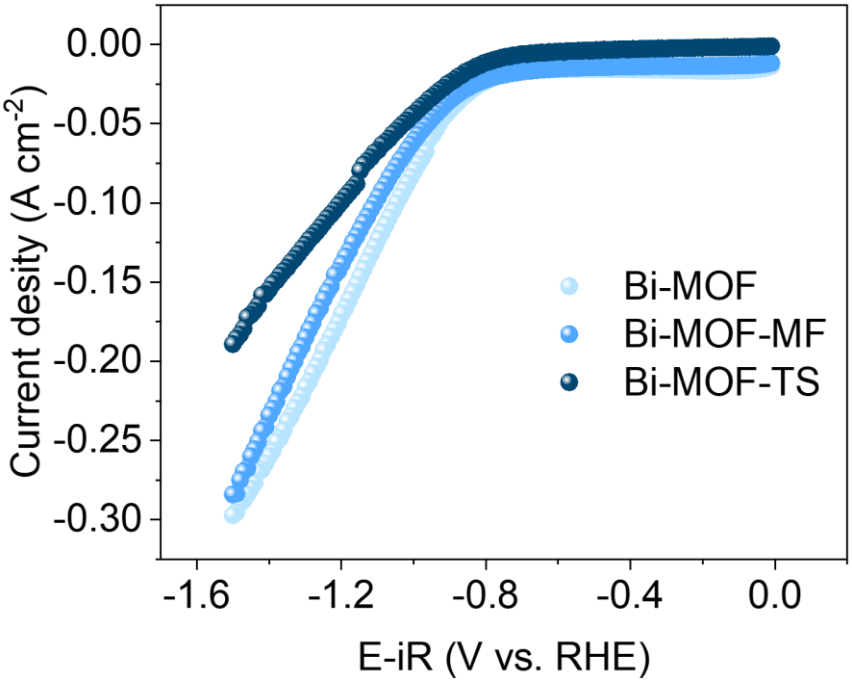

Supplementary Fig. 24| LSV curves of Bi-MOF, Bi-MOF-MF and Bi-MOF-TS without CO_2. 3 Ω iR correction was applied. Source data are provided as a Source Data file.

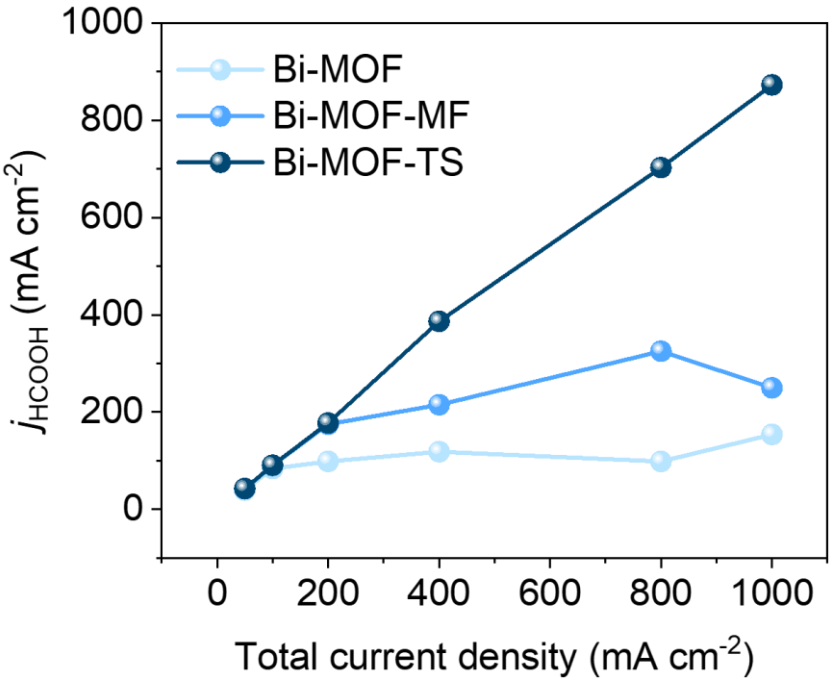

Supplementary Fig. 25| Partial current density of HCOOH under different applied currents for Bi-MOF, Bi-MOF-MF and Bi-MOF-TS in acidic electrolyte. IR correction was not applied. Source data are provided as a Source Data file.

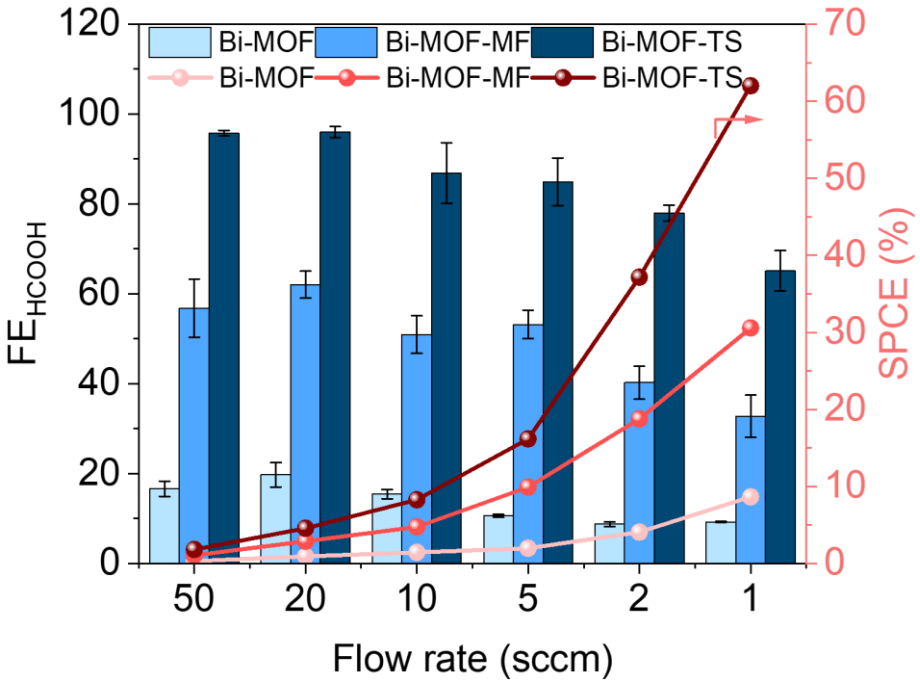

Supplementary Fig. 26| FE of HCOOH and SPCE of CO_2 for the three catalysts at various CO_2 flow rates at 500 mA cm^{-2}. The electrolyte was 0.1 M K_2SO_4+0.02 M H_2SO_4. IR correction was not applied. Source data are provided as a Source Data file.

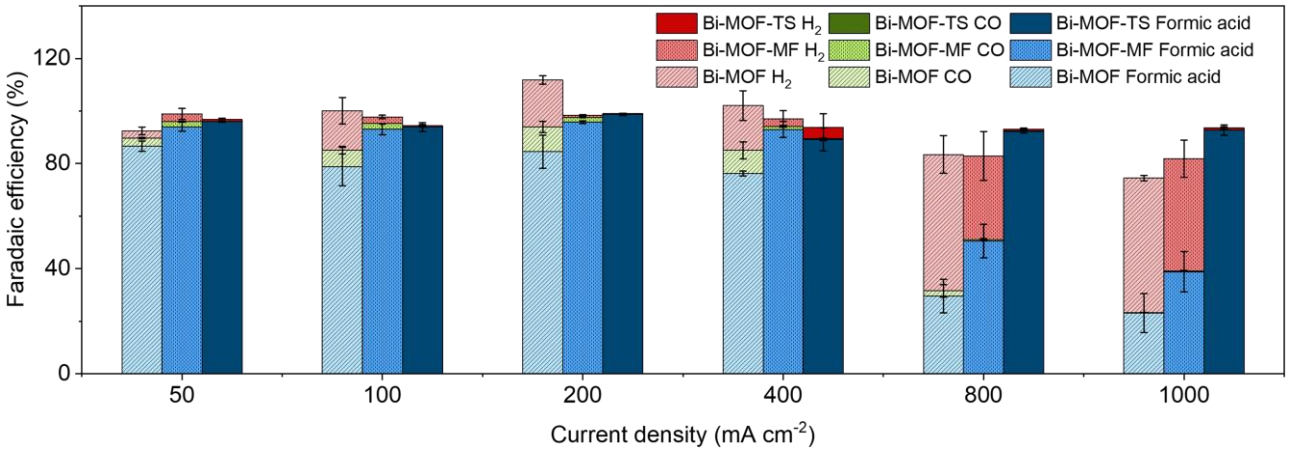

Supplementary Fig. 27| The FE of HCOOH and H_2, CO a for Bi-MOF, Bi-MOF-MF and Bi-MOF-TS in 1 M $KHCO_3$. IR correction was not applied. Source data are provided as a Source Data file.

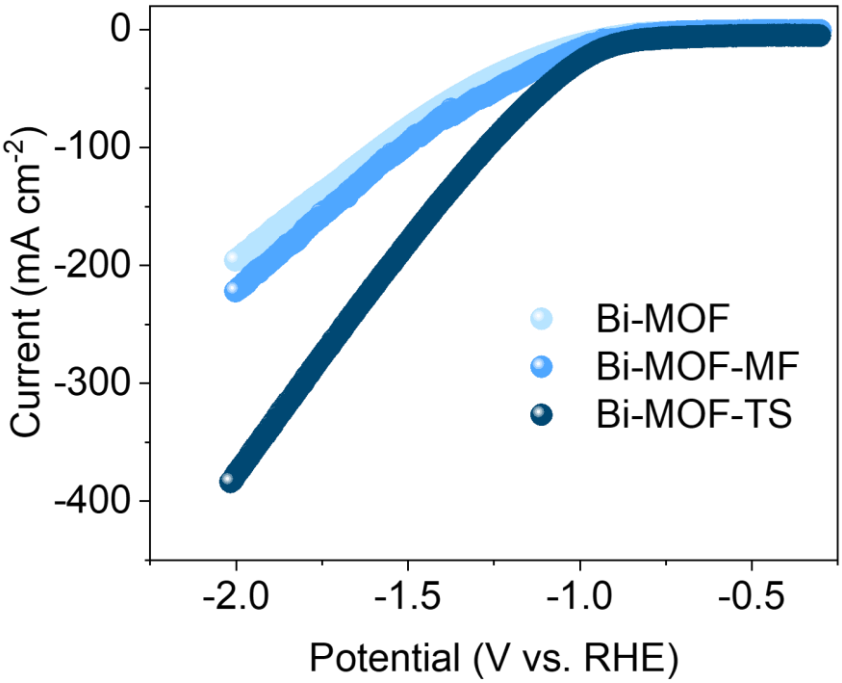

Supplementary Fig. 28| LSV curves of Bi-MOF, Bi-MOF-MF and Bi-MOF-TS in neutral electrolyte at the rate of 10 mV cm^{-1}. No IR correction was performed. Source data are provided as a Source Data file.

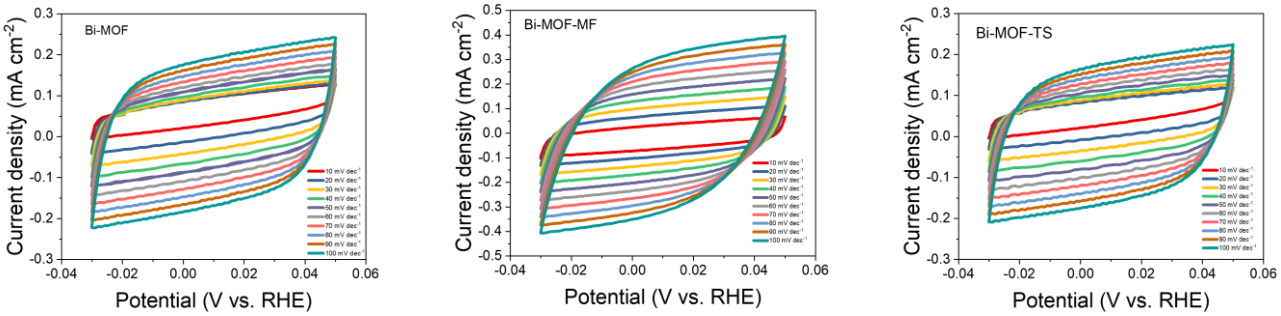

Supplementary Fig. 29| The CV curves with different scan rate under the potential of -0.03 V – 0.05 V vs. RHE of Bi-MOF, Bi-MOF-MF, Bi-MOF-TS. The catalysts ink was mixed with then coated on glassy carbon electrode and run the CV in 1 M $KHCO_3$. Source data are provided as a Source Data file.

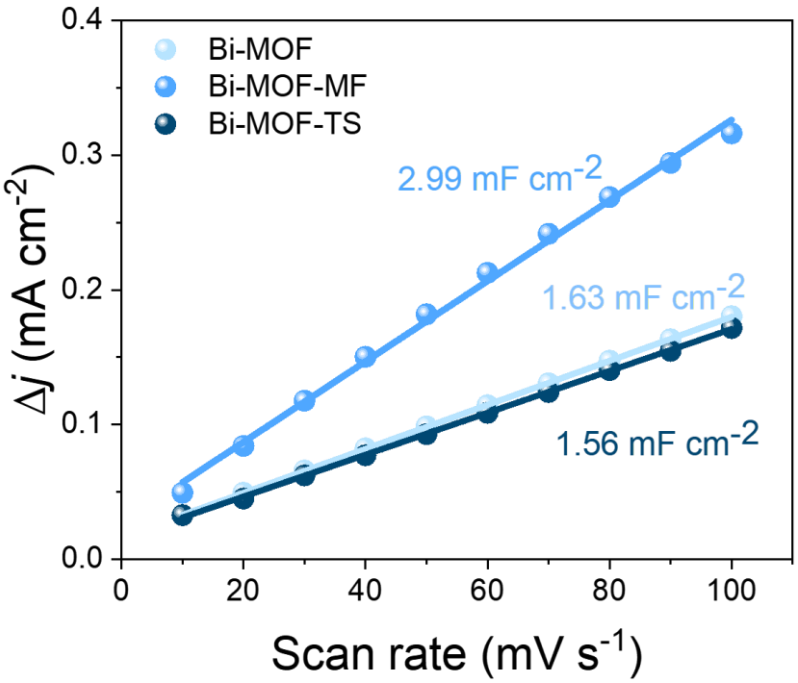

Supplementary Fig. 30| Δj at 0.01 V vs. RHE as a function of the scan rate to evaluate C_{dl}. Source data are provided as a Source Data file.

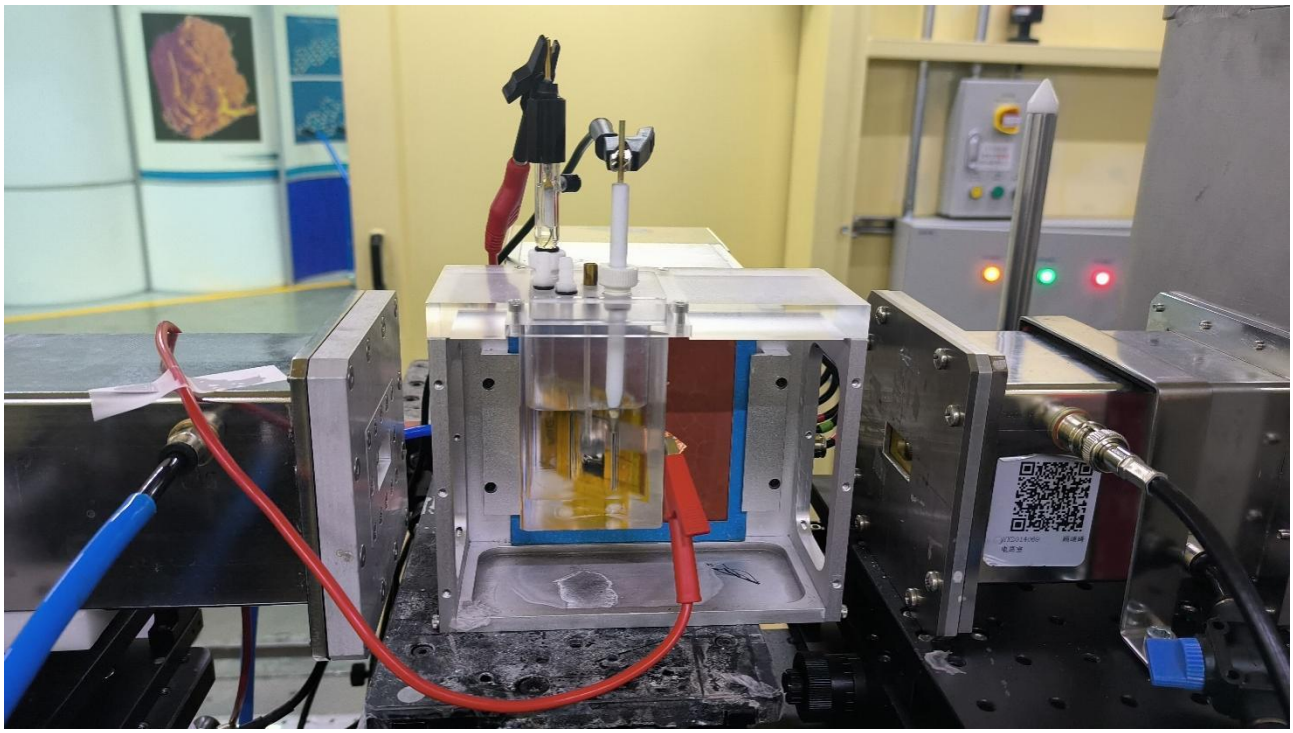

Supplementary Fig. 31| Optical photograph for in-situ XAFS measurements.

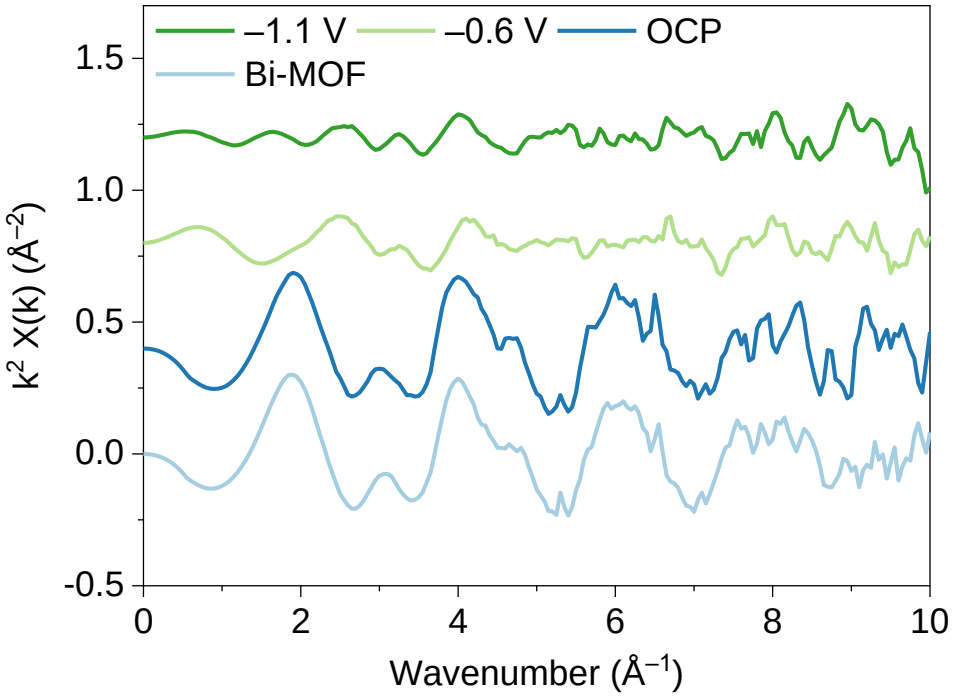

Supplementary Fig. 32| K-space of Bi-MOF under in-situ test. Source data are provided as a Source Data file.

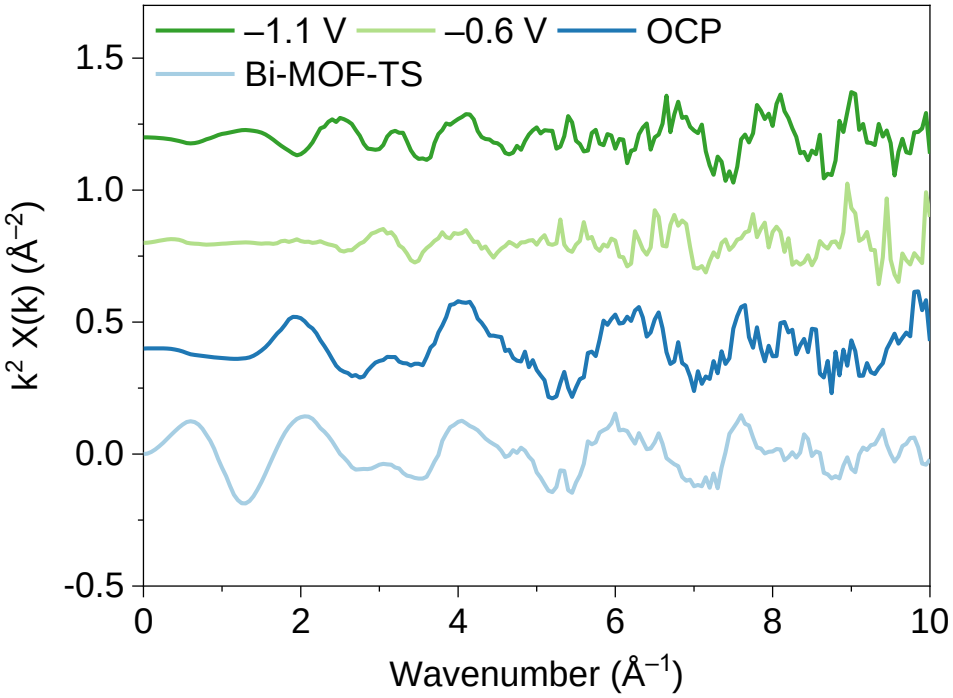

Supplementary Fig. 33| K-space of Bi-MOF-TS under in-situ test. Source data are provided as a Source Data file.

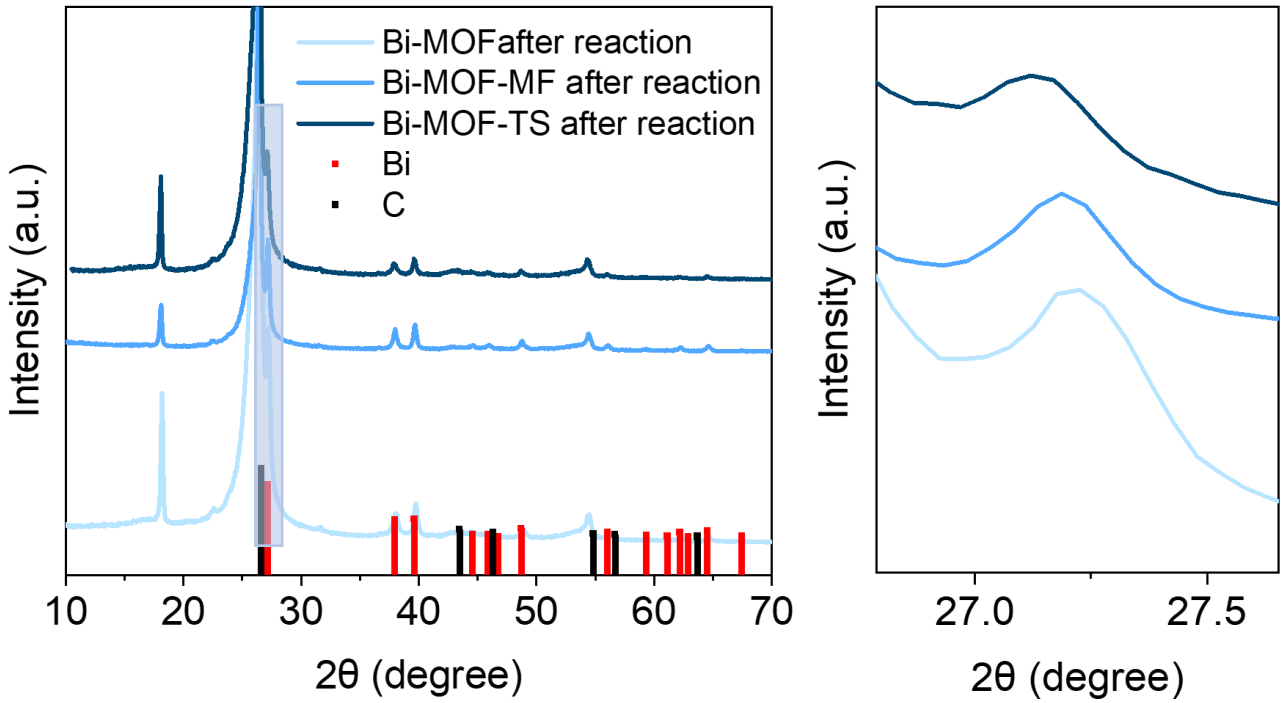

Supplementary Fig. 34| XRD of three kinds of pre-catalysts after CO_2RR and the enlarged image of the diffraction peak at the 012 crystal plane. Source data are provided as a Source Data file.

We calculate strain(s) through the formula:

$$s = (l_f - l_i)/l_i * 100\%$$

where l_f and l_i represent the interplanar spacing calculated by XRD of the initial and final states, respectively.

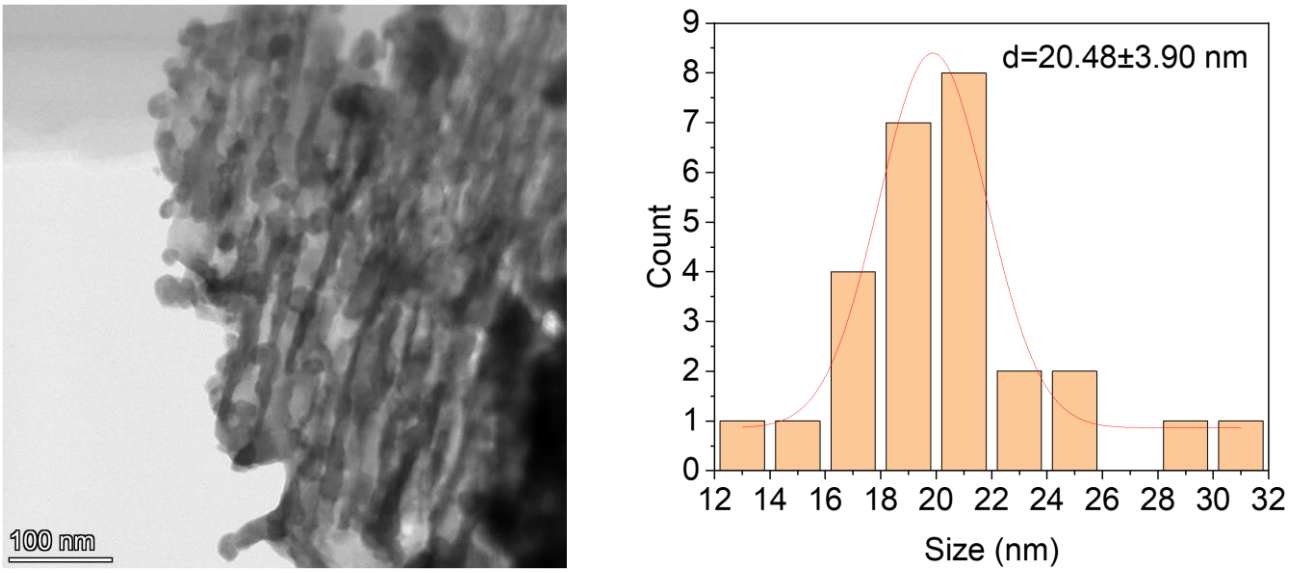

Supplementary Fig. 35| HAADF-STEM image of Bi-MOF-TS-derived Bi^0 and the size distribution for Bi particles in it.

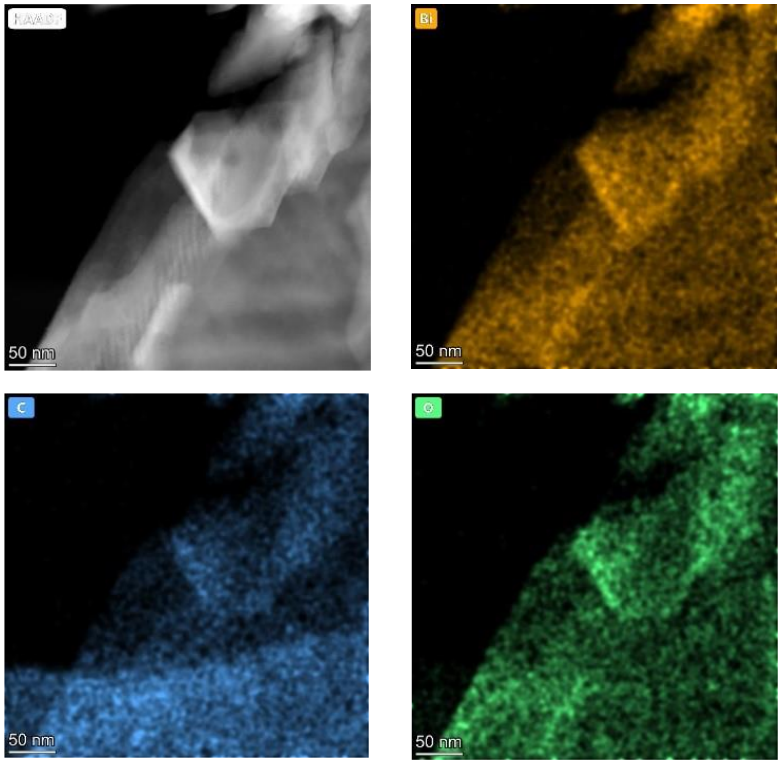

Supplementary Fig. 36| High-angle annular dark-field scanning transmission electron microscopy (HAADF-STEM) image and Energy Dispersive X-ray spectroscopy (EDX) mapping of the Bi-MOF after reaction.

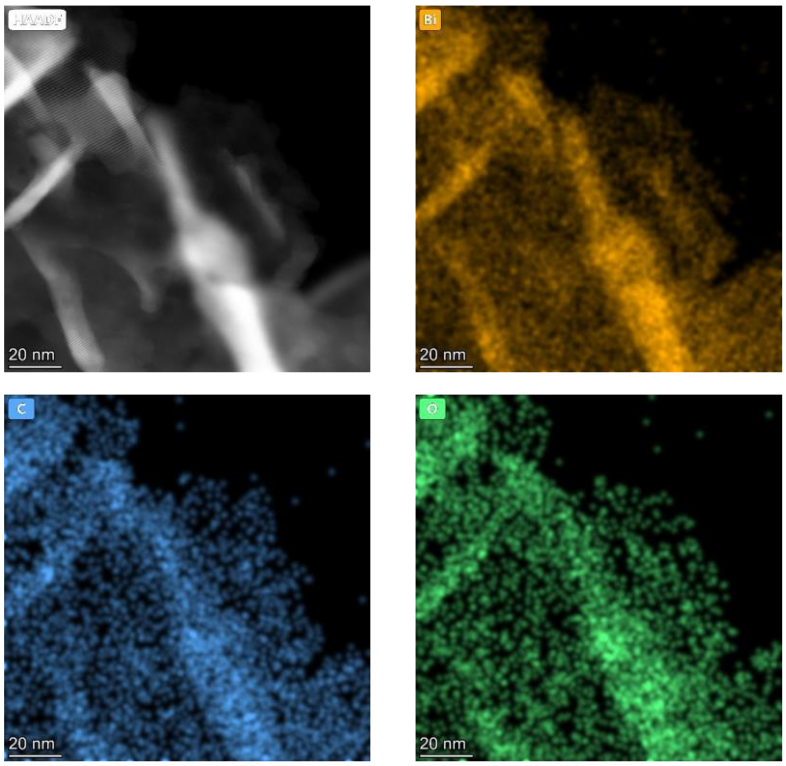

Supplementary Fig. 37| High-angle annular dark-field scanning transmission electron microscopy (HAADF-STEM) image and Energy Dispersive X-ray spectroscopy (EDX) mapping of the Bi-MOF-MF after reaction.

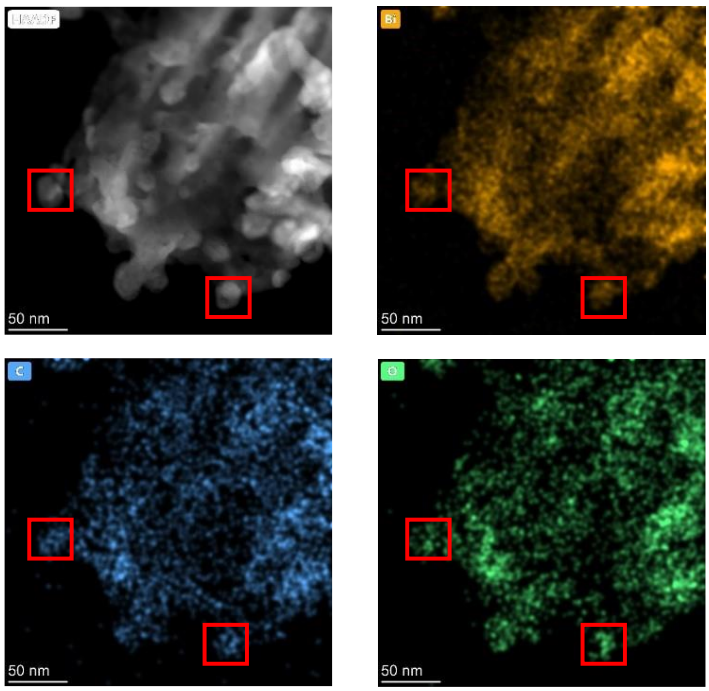

Supplementary Fig. 38| High-angle annular dark-field scanning transmission electron microscopy (HAADF-STEM) image and Energy Dispersive X-ray spectroscopy (EDX) mapping of the Bi-MOF-TS after reaction.

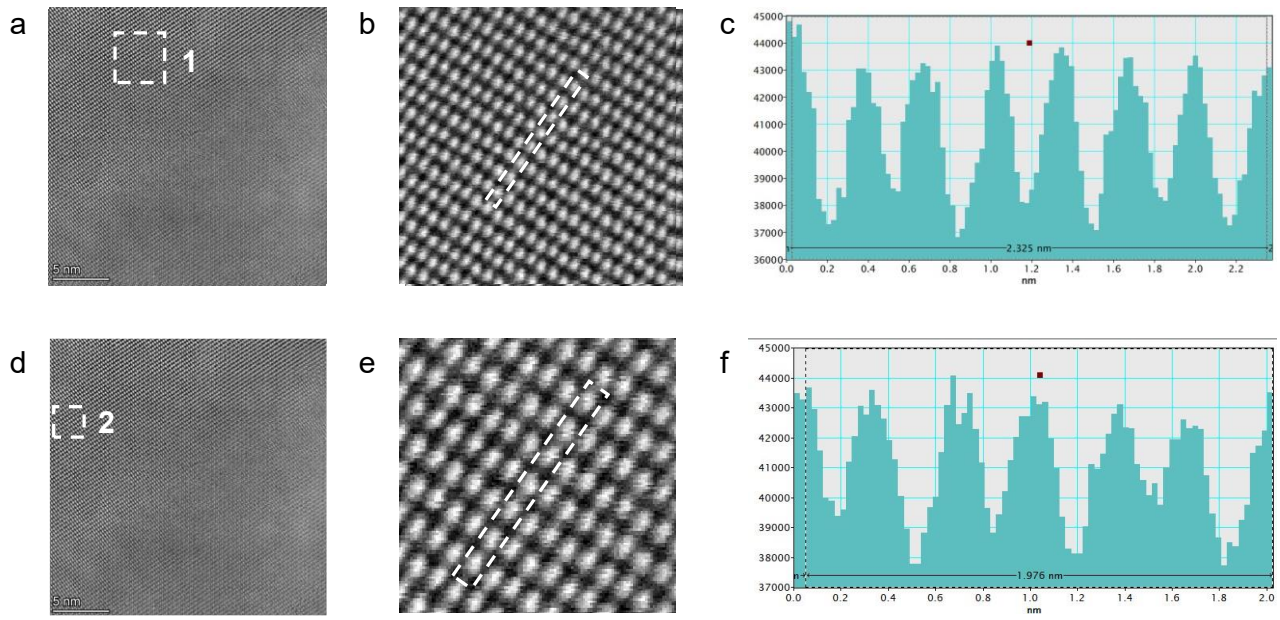

Supplementary Fig. 39| High-angle annular dark-field scanning transmission electron microscopy (HAADF-STEM) images. (a, d) the image of Bi-MOF after reaction, (b) the partial zoom of STEM image at 1st position, (c) the atomic distance of the Bi (012) facet at 1st position, (e) the partial zoom of STEM image at 2nd position, (f) the atomic distance of the Bi (012) facet at 2nd position.

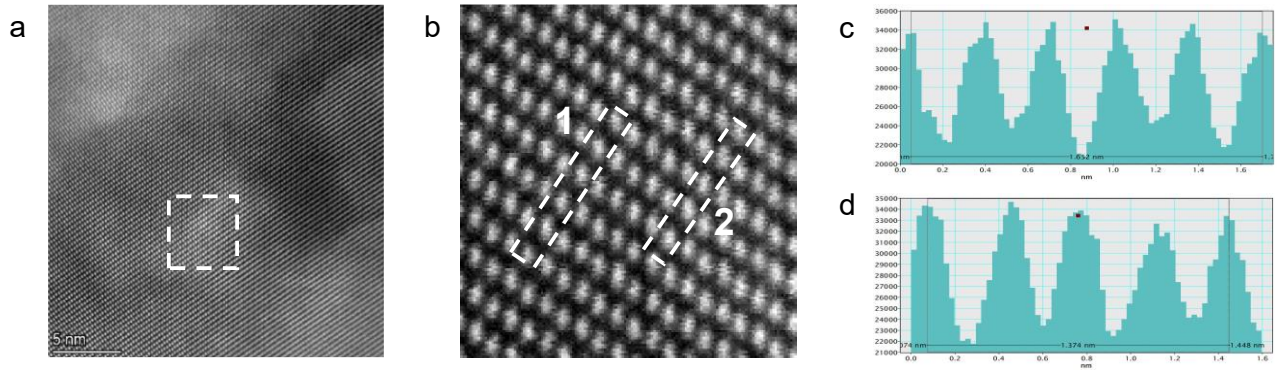

Supplementary Fig. 40| High-angle annular dark-field scanning transmission electron microscopy (HAADF-STEM) images. (a) the image of Bi-MOF-MF after reaction, (b) the partial zoom of STEM image, (c-d) the atomic distance of the Bi (012) facet, (c) the 1st position and (d) the 2nd position.

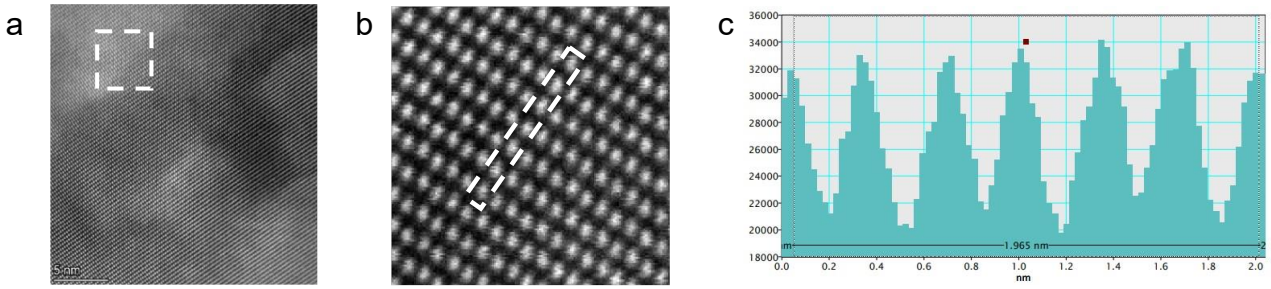

Supplementary Fig. 41| High-angle annular dark-field scanning transmission electron microscopy (HAADF-STEM) images. (a) the image of Bi-MOF-MF after reaction, (b) the partial zoom of STEM image at another position, (c) the atomic distance of the Bi (012) facet.

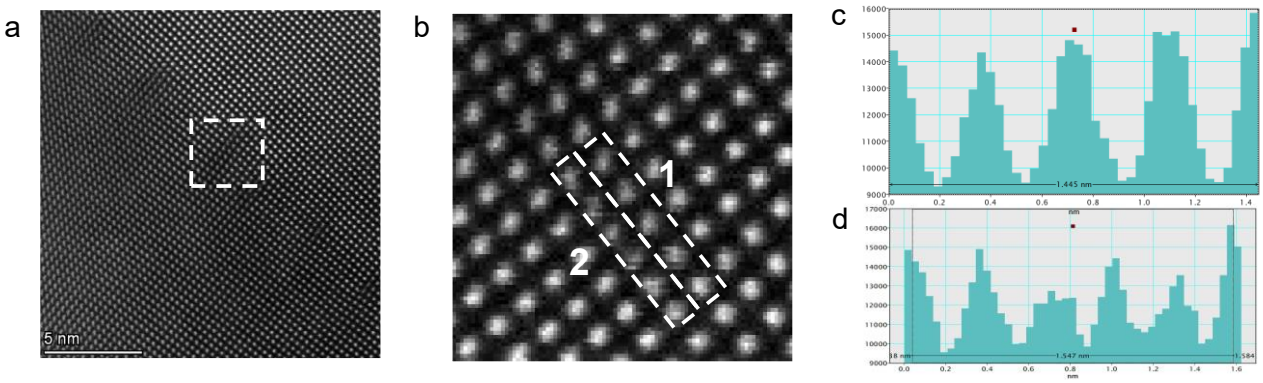

Supplementary Fig. 42| High-angle annular dark-field scanning transmission electron microscopy (HAADF-STEM) images. (a) the image of Bi-MOF-TS after reaction, (b) the partial zoom of STEM image at the SV position, (c-d) the atomic distance of the Bi (012) facet, (c) the 1st position is the place with tensile strain and (d) the 2nd position is the place with compressive strain.

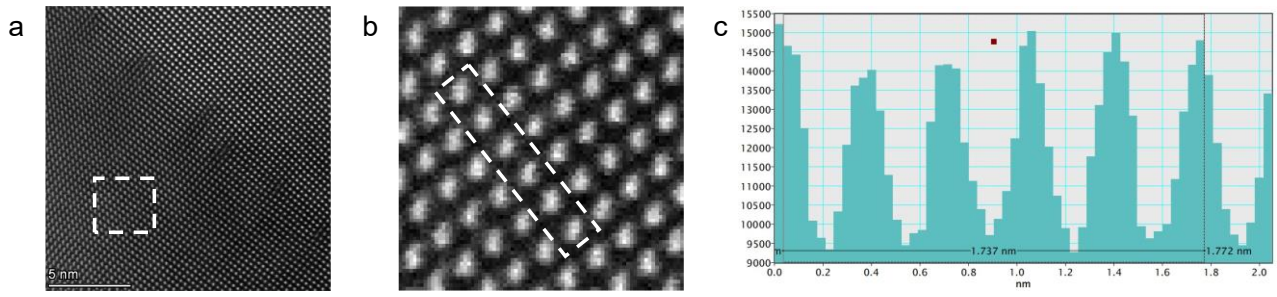

Supplementary Fig. 43| High-angle annular dark-field scanning transmission electron microscopy (HAADF-STEM) images. (a) the image of Bi-MOF-TS after reaction, (b) the partial zoom of STEM image at a normal position, (c) the atomic distance of the Bi (012) facet.

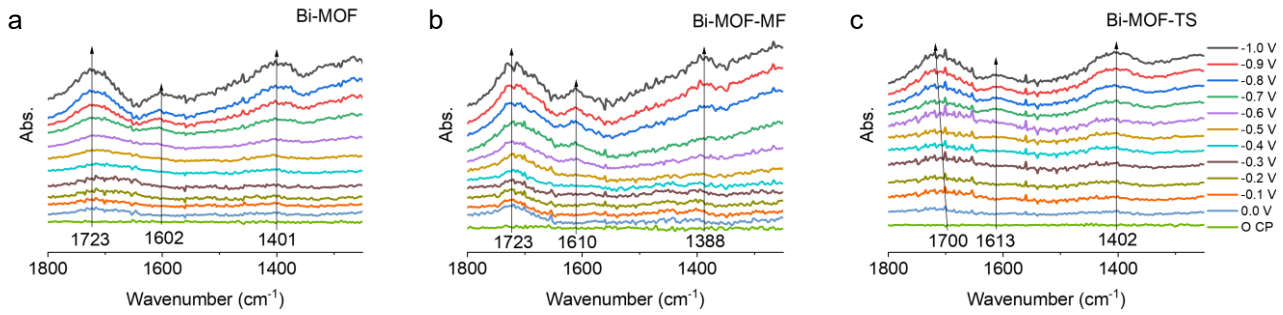

Supplementary Fig. 44| In-situ ATR-SEIRAS spectra of Bi-MOF(a) and Bi-MOF-MF(b) Bi-MOF-TS(c) at the different applied potentials (reference to RHE). Source data are provided as a Source Data file.

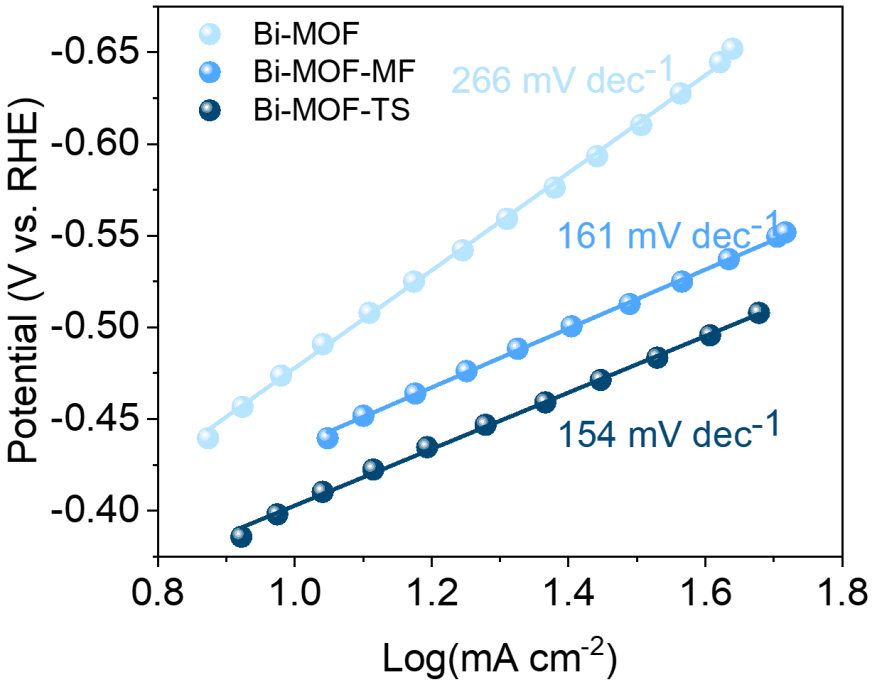

Supplementary Fig. 45| Tafel plots for the Bi-MOF, Bi-MOF-MF and Bi-MOF-TS. Source data are provided as a Source Data file.

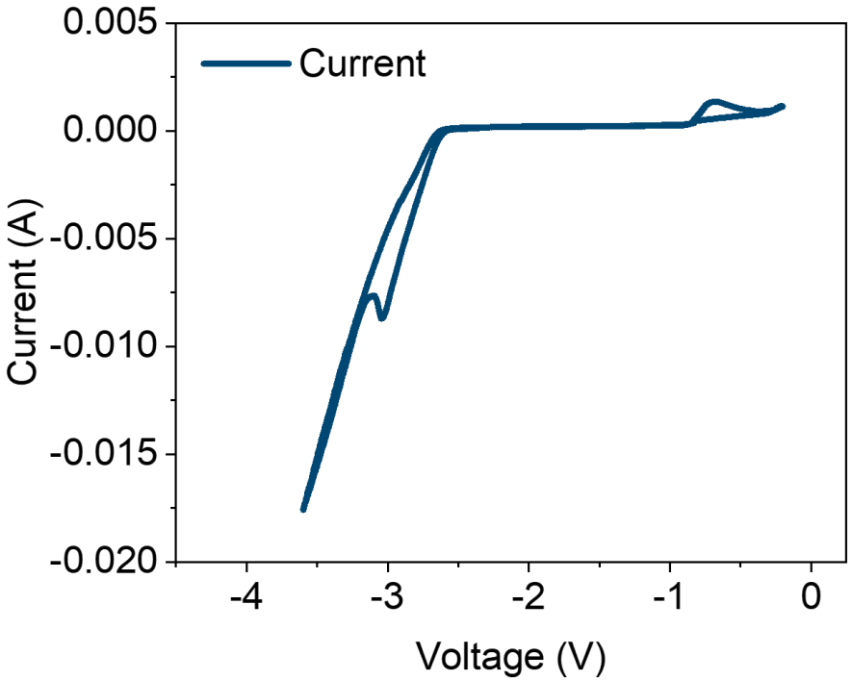

Supplementary Fig. 46| The CV cycle of Zn-CO_2 battery at a scan rate of 10 mV s^{-1}. Source data are provided as a Source Data file.

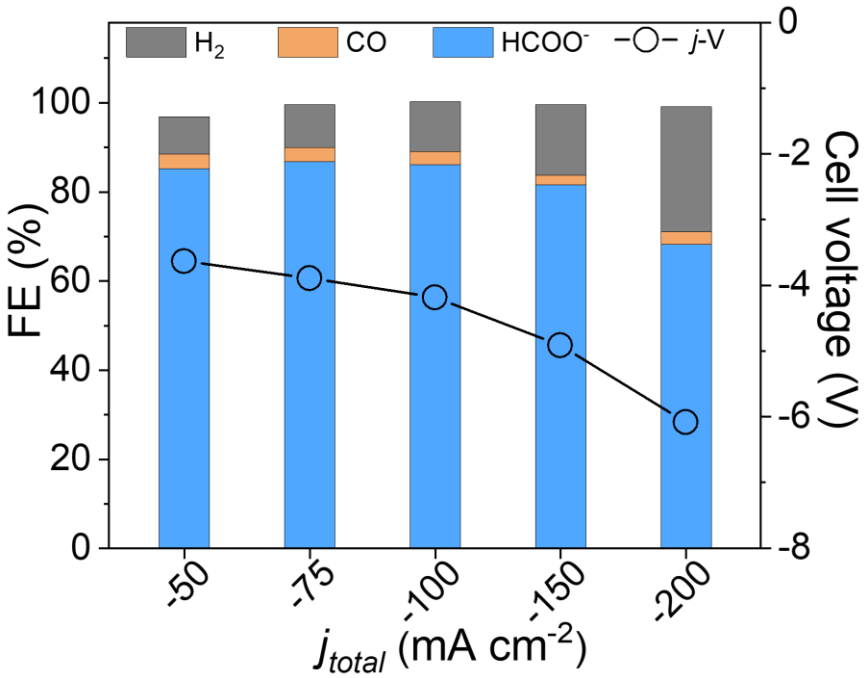

Supplementary Fig. 47| The cell voltage and FE of HCOOH, H_2, and CO for the Bi-MOF-TS at different current densities. Source data are provided as a Source Data file.

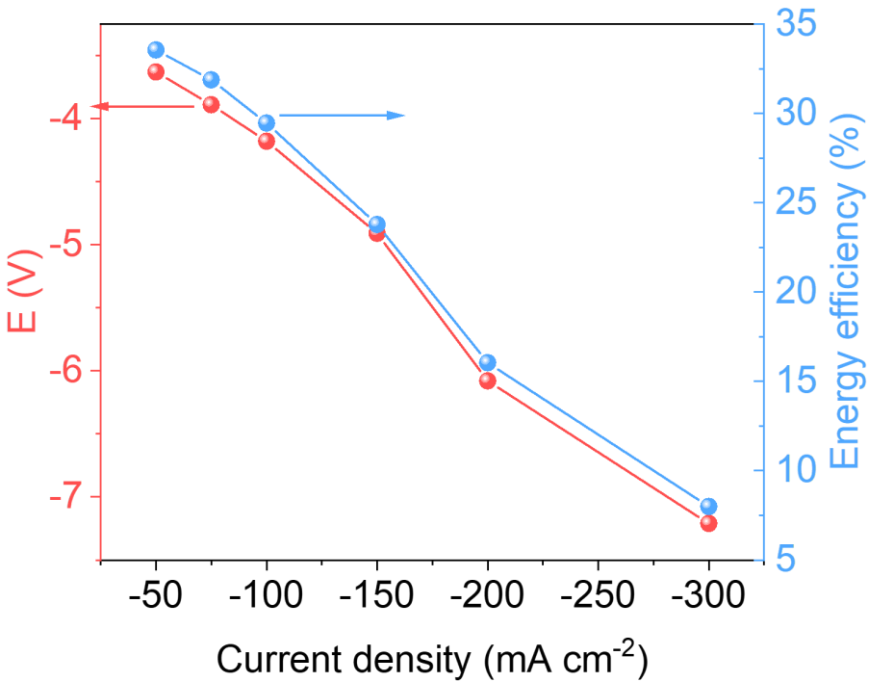

Supplementary Fig. 48| The total cell voltage and energy efficiency of formic acid as a function of current density. Source data are provided as a Source Data file.

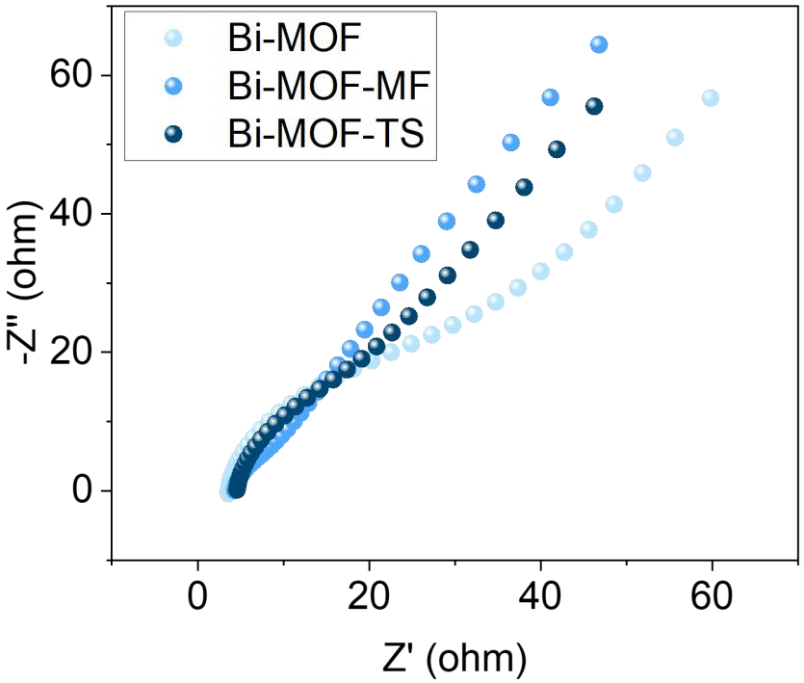

Supplementary Fig. 49| EIS tests in alkaline electrolyte. Source data are provided as a Source Data file.

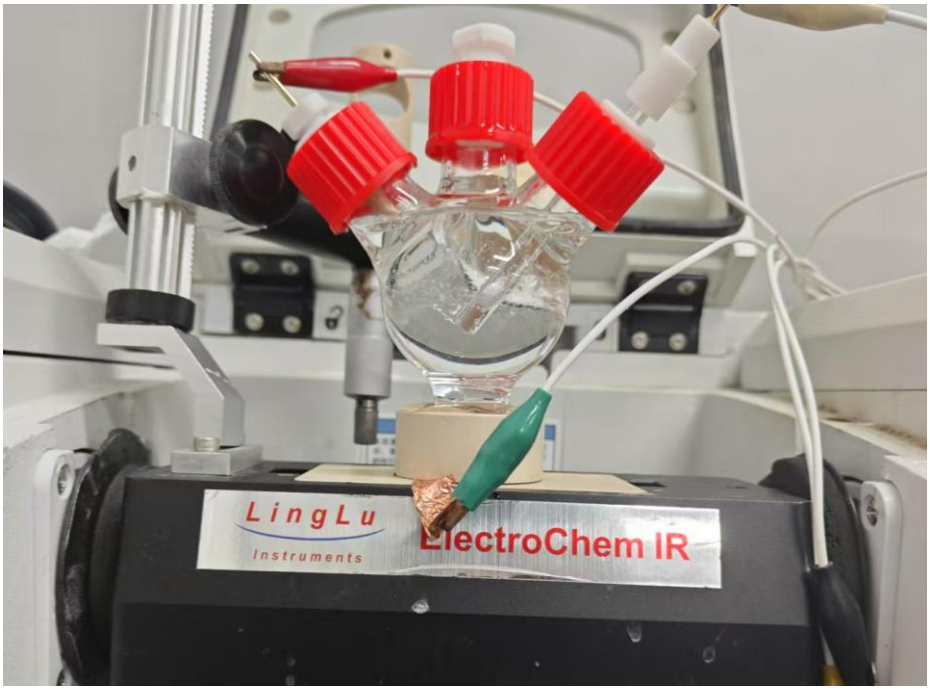

Supplementary Fig. 50| Optical photograph for in-situ ATR-SEIRAS measurements.

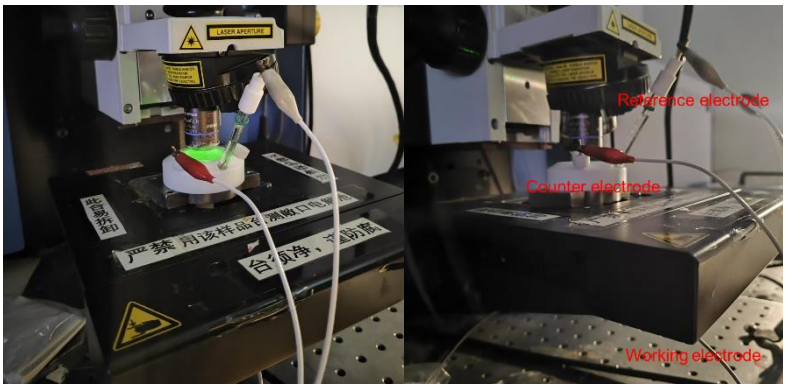

Supplementary Fig. 51| Optical photograph for in-situ Raman measurements.

Table S1 Strain and ΔG_{*OCHO} of Bi sites (2-5) on Bi-1SV, Bi-2SV, and Bi-3SV.

	Strain / %				**ΔG_{*OCHO} / eV**			
	Site 2	**Site 3**	**Site 4**	**Site 5**	**Site 2**	**Site 3**	**Site 4**	**Site 5**
Bi-1SV	2.59%	1.58%	0.88%	0.49%	0.58	0.82	1.00	1.20
Bi-2SV	3.19%	1.40%	0.98%	0.60%	0.53	0.92	0.97	1.13
Bi-3SV	2.84%	1.55%	1.14%	0.89%	0.24	0.92	1.04	1.05

Table S2. EXAFS fitting results of Bi-MOF-MF and Bi-MOF-TS.

Sample	Path	CN	R (Å)	σ^2 (10^{-3} Å^2)	S_0^2	R- factor
Bi-MOF-MF	Bi–O	4.48 ± 0.53	2.18 ± 0.01	6.45 ± 1.7	0.224 ± 0.027	0.0189
Bi-MOF-TS	Bi–O	3.2 ± 0.79	2.23 ± 0.02	3.09 ± 0.13	0.256 ± 0.04	0.0402

Table S3. Comparison of the potential range with Bi-based electrocatalysts recently reported – a high formate selectivity and the highest partial current density of formate for the Bi-MOF-MF and Bi-MOF-TS developed in this study.

Ref.	Catalysts	Electrolytes	Potential range with formate selectivity over 90%	Highest partial current density of formate (mA cm^{-2})	FE (%)	Reference
	Bi-MOF-TS	1 M KOH	800 mV	-995	99%	This work
	Bi-MOF-MF	1 M KOH	600 mV	-642	98%	This work
1	2D-Bi[1]	2 M KOH	70 mV (-0.57 V~-0.64 V)	–215	86%	Nature Energy, 2019, 4, 9, 776-785
2	Defective Bi nanotubes[2]	1 M KOH	——	–206	98%	Nat. Commun., 2019, 10, 2807-2816
3	Bi NSs[3]	1 M KOH	200 mV (-0.48 V~-0.67 V)	–360	89	Advanced Energy Materials, 2020, 10, 36, 2001709
4	Bismuthene nanosheets[4]	1 M KHCO3	750 mV (-0.65 V~-1.4 V)	–273	86%	Advanced Functional Materials, 2021, 31, 4, 2006704
5	Bi_2O_3@C-800[5]	1 M KOH	700 mV (-0.4 V~-1.1 V)	–208	92%	Angewandte Chemie, 2020, 132, 27, 10899-10905
6	Bi RDs[6]	1 M KOH	360 mV (-0.42 V~-0.78 V)	–289	94%	Advanced Materials, 2021, 33, 31, 2008373
7	Bi-ene-NW[7]	1 M KOH	400 mV (-0.57 V~-0.97 V)	–515	92%	Energy & Environmental Science, 2021, 14, 9, 4998-5008
8	BOC@GDY[8]	1 M KOH	450 mV (-0.65 V~-1.1 V)	–200	93.5%	Science Bulletin, 2021, 66, 15, 1533-1541
9	Bi nanoribbons[9]	1 M KOH	550 mV (-0.75 V~-1.3 V)	–193	95%	ACS Energy Letters, 2022, 7, 4, 1454-1461

10	Cu-Bi structure[10]	0.5 M $KHCO_3$	300 mV (-0.9 V~-1.1 V)	-76	92.5%	Angewandte Chemie, 2023, 62, 11, e202217569.
11	Bi nanoflowers[11]	0.1 M $KHCO_3$	200 mV (-0.8 V~-1.0 V)	-26	92.3%	Advanced Functional Materials, 2023, 2301984.
12	$(BiO)_2CO_3$[12]	5 M KOH	——	–1353.4	85%	ACS Catal., 2022, 12, 17, 10872–10886
13	BiOBr[13]	1 M $KHCO_3$	300 mV (-0.9 V~-1.1 V)	-148	90%	Nature Catalysis, 2023, 6, 9, 796-806.
14	BS/VC[14]	1M KOH	1200 mV (-0.7 V~-1.8 V)	-910	94%	Nature Commun., 2023, 14, 1, 4670.
15	BBS[15]	1M KOH	400 mV (-0.7 V, -0.9 V~-1.2 V)	-250	95%	Angewandte Chemie, 2023, e202303117.

Table S4. Comparison of the highest HCOOH faradic efficiency for HCOOH and the highest partial current density for HCOOH with Bi-based electrocatalysts recently reported.

Ref.	catalyst	pH	Highest partial current density of formate (mA cm^{-2})	FE (%)	Referennce
	Bi-MOF-TS	1.5	872.7	96.6%	This work
	Bi-MOF-MF	1.5	325.2	90.2%	This work
16	BiOCl[16]	2	20	91%	Journal of the American Chemical Society, 2024, 146, 8, 5333–5342.
17	Bimetallic Cu-Bi[17]	2	98	91%	Angewandte Chemie, 2023, 62, 11, e202217569.
18	Bi nanosheets[18]	0.5	237.11	92.2%	ACS Catalysis, 2022, 12, 4, 2357–2364.
19	D-Bi[19]	1	100	77.1%	ChemElectroChem, 2024, 11, 7, e202300799.
20	TDPE-PPSU Bi[20]	1.8	63.6	85.2%	Small, 2023, 19, 23, 2207650.

Table S5. Comparison of peak power densities of recently reported Zn-CO_2 batteries with formate as the reduction product.

Ref.	Catalyst	Peak power density (mW cm^{-2})	Reference
	Bi-MOF-TS	21.4 mW cm^{-2}	This work
21	Bi_2S_3–PPy	2.4 mW cm^{-2}	Energy & Environmental Science, 2023,16, 3885-3898.[21]
22	s-SnLi	1.24 mW cm^{-2}	Angewandte Chemie, 2021, 133, 49, 25945-25949.[22]
23	Bi-PNCB	1.43 mW cm^{-2}	Nano Energy, 2022, 92, 106780.[23]
24	BiC/HCS	7.2 ± 0.5 mW cm^{-2}	Applied Catalysis B: Environment and Energy, 2022, 307, 15, 121145.[24]

References

1. Xia C*, et al.* Continuous production of pure liquid fuel solutions via electrocatalytic CO_2 reduction using solid-electrolyte devices. *Nat. Energy* **4**, 776-785 (2019).

2. Gong Q*, et al.* Structural defects on converted bismuth oxide nanotubes enable highly active electrocatalysis of carbon dioxide reduction. *Nat. Commun.* **10**, 2807 (2019).

3. Yang J*, et al.* Bi-Based Metal-Organic Framework Derived Leafy Bismuth Nanosheets for Carbon Dioxide Electroreduction. *Adv. Energy Mater.* **10**, 2001709 (2020).

4. Ma W*, et al.* Monoclinic Scheelite Bismuth Vanadate Derived Bismuthene Nanosheets with Rapid Kinetics for Electrochemically Reducing Carbon Dioxide to Formate. *Adv. Funct. Mater.* **31**, 2006704 (2020).

5. Deng P*, et al.* Metal–Organic Framework-Derived Carbon Nanorods Encapsulating Bismuth Oxides for Rapid and Selective CO_2 Electroreduction to Formate. *Angew. Chem. Int. Edit.* **59**, 10807-10813 (2020).

6. Xie H*, et al.* Facet Engineering to Regulate Surface States of Topological Crystalline Insulator Bismuth Rhombic Dodecahedrons for Highly Energy Efficient Electrochemical CO_2 Reduction. *Adv. Mater.* **33**, 2008373 (2021).

7. Zhang M*, et al.* Engineering a conductive network of atomically thin bismuthene with rich defects enables CO_2 reduction to formate with industry-compatible current densities and stability. *Energ. Environ. Sci.* **14**, 4998-5008 (2021).

8. Tang S-F, Lu X-L, Zhang C, Wei Z-W, Si R, Lu T-B. Decorating graphdiyne on ultrathin bismuth subcarbonate nanosheets to promote CO_2 electroreduction to formate. *Sci. Bull.* **66**, 1533-1541 (2021).

9. Li Y*, et al.* In Situ Confined Growth of Bismuth Nanoribbons with Active and Robust Edge Sites for Boosted CO_2 Electroreduction. *ACS Energy Lett.* **7**, 1454-1461 (2022).

10. Li Z*, et al.* Electron-Rich Bi Nanosheets Promote $CO2^{\cdot-}$ Formation for High-Performance and pH-Universal Electrocatalytic CO_2 Reduction. *Angew. Chem. Int. Edit.* **62**, e202217569 (2023).

11. Yang S*, et al.* In Situ Structure Refactoring of Bismuth Nanoflowers for Highly Selective Electrochemical Reduction of CO_2 to Formate. *Adv. Funct. Mater.* **33**, (2023).

12. Montiel IZ, Dutta A, Kiran K. CO_2 Conversion at High Current Densities: Stabilization of Bi(III)-Containing Electrocatalysts under CO_2 Gas Flow Conditions. *ACS Catal.* **12**, 10872–10886 (2022).

13. Yang S*, et al.* Halide-guided active site exposure in bismuth electrocatalysts for selective CO_2 conversion into formic acid. *Nat. Catal.* **6**, 796-806 (2023).

14. Zhu J*, et al.* Surface passivation for highly active, selective, stable, and scalable CO_2 electroreduction. *Nat.*

Commun. **14**, 4670 (2023).

15. Lv L*, et al.* Coordinating the Edge Defects of Bismuth with Sulfur for Enhanced CO_2 Electroreduction to Formate. *Angew. Chem. Int. Edit.* **62**, e202303117 (2023).

16. Liu H*, et al.* Observation on Microenvironment Changes of Dynamic Catalysts in Acidic CO_2 Reduction. *J. Am. Chem. Soc.* **146**, 5333-5342 (2024).

17. Li Z*, et al.* Electron-Rich Bi Nanosheets Promotes CO_2- Formation for High-Performance and pH-Universal Electrocatalytic CO_2 Reduction. *Angewandte Chemie (International ed. in English)* **62**, e202217569 (2023).

18. Qiao Y*, et al.* Engineering the Local Microenvironment over Bi Nanosheets for Highly Selective Electrocatalytic Conversion of CO_2 to HCOOH in Strong Acid. *ACS Catal.* **12**, 2357-2364 (2022).

19. Lhostis F, Tran N-H, Rousse G, Zanna S, Menguy N, Fontecave M. Promoting Selective CO_2 Electroreduction to Formic Acid in Acidic Medium with Low Potassium Concentrations under High CO_2 Pressure. *Chem. Electro. Chem.* **11**, e202300799 (2024).

20. Yan T, Pan H, Liu Z, Kang P. Phase-Inversion Induced 3D Electrode for Direct Acidic Electroreduction CO_2 to Formic acid. *Small* **19**, 2207650 (2023).

21. Li C*, et al.* Bio-inspired engineering of Bi_2S_3–PPy composite for the efficient electrocatalytic reduction of carbon dioxide. *Energ. Environ. Sci.* **16**, 3885-3898 (2023).

22. Yan S*, et al.* Electron localization and lattice strain induced by surface lithium doping enable ampere‐level electrosynthesis of formate from CO_2. *Angew. Chem. Int. Edit.* **133**, 25945-25949 (2021).

23. Wang Y*, et al.* Electron accumulation enables Bi efficient CO2 reduction for formate production to boost clean Zn-CO_2 batteries. *Nano Energy,* **92**, 106780 (2022).

24. Yang M*, et al.* Highly dispersed Bi clusters for efficient rechargeable Zn−CO_2 batteries. *Appl. Catal. B: Environ.*, **307**, 121145 (2022).